



STScI | SPACE TELESCOPE
SCIENCE INSTITUTE

WFC3 Instrument Science Report 2021-04

New time-dependent WFC3 UVIS inverse sensitivities

Annalisa Calamida, Jennifer Mack, Jennifer Medina, Clare Shahanan, Varun Bajaj, Susana Deustua

February 11, 2021

ABSTRACT

We present new time-dependent WFC3 UVIS1 and UVIS2 inverse sensitivities for the 42 filters covering both detectors. The new values were calculated using photometry collected from 2009 to 2019 for five CALSPEC standards, the white dwarfs GRW+70 5824, GD 153, GD 71, G191B2B, and the G-type star P330E. Using these data, we compute sensitivity changes for each detector and filter and normalize the observed count rates of the standard stars to a reference time in 2009. The new set of inverse sensitivity values use new standard star models and an updated reference spectral energy distribution for Vega. By correcting for sensitivity changes with time, we derive improved detector sensitivity ratios and new encircled energy values for several filters. At the same time we update the inverse sensitivities for the 20 quad filters using the new models for the standard stars and Vega. However, for these filters no time-dependent sensitivity changes are calculated. The new inverse sensitivities provide a photometric internal precision better than 0.5% for wide-, medium-, and narrow-band filters, and 5% for quad filters, a considerable improvement from the latest 2017 calibration. The new time-dependent inverse sensitivities are populated as photometric keywords in the image headers as of October 15, 2020.

1 Introduction

The Wide Field Camera 3 (WFC3) UVIS channel consists of two detectors (alternatively referred as chips in WFC3 documentation), UVIS1 and UVIS2, with unique quantum efficiencies and sensitivities changing with time at a different rate (Gosmeyer et al. 2016, Shanahan et al. 2017, Khadraka et al. 2018). One result is that the count rate ratio of the two detectors changes with time.

In 2016, the WFC3 team implemented a chip-dependent photometric calibration and new values of the inverse sensitivities for UVIS1 and UVIS2 were provided (Deustua et al. 2016, hereinafter DE16), and later improved by using updated models (Deustua et al. 2017, hereinafter DE17); however, these values assumed constant sensitivity with time. As documented in Khandrika et al., sensitivity changes up to 0.2% per year, depending on the filter and the detector, results in differences of more than 2% in flux between 2009, when WFC3 was installed, and the current epoch. Due to the sensitivity changes being different for UVIS1 and UVIS2, as well as small errors in the flat field between different amplifiers, the current count rate ratio of the two detectors may be different by as much as 2% (Mack et al. 2016, Calamida et al. 2018).

Furthermore, the models for the HST primary spectrophotometric standard white dwarfs (WDs), GD153, GD71 and G191B2B, provided by the CALSPEC calibration database¹, were updated in March 2020 (Bohlin et al. 2020, hereinafter BO20). Also, the Vega reference grey flux at 0.5556 μm , as reconciled with the MSX mid-IR absolute flux measures, increased by $\approx 0.9\%$ ². The standard WD absolute fluxes are determined by the normalization of their modeled spectral energy distributions (SEDs) by their respective relative responses to Vega, using STIS precision spectrophotometry of all four stars, Vega, G191B2B, GD153 and GD71, and the $3.47 \times 10^{-9} \text{ erg} \cdot \text{cm}^{-2} \cdot \text{s}^{-1} \cdot \text{\AA}^{-1}$ flux of Vega at 0.5556 μm . This method provides the basis for *HST*'s entire calibration system. With the adoption of the new models presented in BO20, the HST primary standard WD absolute fluxes increased overall by $\approx 2\%$ for wavelengths in the range 0.15 - 0.4 μm , and $\approx 1.5\%$ in the range 0.4 - 1 μm . **Therefore, WFC3 inverse sensitivities need to be updated with the new CALSPEC reference fluxes (CALSPECv11), and also to take into account the sensitivity changes with time of the UVIS1 and UVIS2 detectors.**

In this ISR we provide new time-dependent UVIS1 and UVIS2 inverse sensitivities for all full-frame (including both detectors) 42 filters, by analyzing 10 years of photometry collected for five CALSPEC standards, the WDs GRW+70 5824, hereinafter GRW70, GD153, GD71, G191B2B, and the G-type star P330E, and using their updated SEDs based on the new CALSPECv11 models. The 20 quad filter inverse sensitivities were also updated to incorporate the new models, but do not include any time-dependent correction since no observations in these filters are currently available beyond 2010.

2 Observations and data reduction

Observations for the four WDs and P330E were collected with WFC3 between June 2009 and November 2019 during regular calibration observations and a few GO programs. The five standard stars were observed in each of the four UVIS 512x512 corner sub-arrays, and the exposure times for each filter were optimized to obtain a minimum Signal-to-Noise ratio (*SNR*) of ≈ 100 , and on average $SNR \approx 500$, per exposure. Table 1 lists the program number of the proposals, the standard star names and filters for the observations included in this work.

¹<https://www.stsci.edu/hst/instrumentation/reference-data-for-calibration-and-tools/astronomical-catalogs/calspec>

²The spectral energy distribution for Vega used in the new calibration is *alpha_Lyr_stis_010.fits*

Table 1: Program number of the regular calibration or GO proposals, standard star name and filter for the observations included in this analysis.

Program	Star	Filters
11426	GRW70	F218W F225W F275W F280N F300X F336W F343N F373N F390M F390W F395N F410M F438W F467M F606W F814W
11450	GD153	F218W F225W F275W F280N F300X F336W F343N F350LPF373N F390M F390W F395N F410M F438W F467M F469N F475W F475X F487N F502N F547M F555W F600LPF606W F621M F625W F656N F658N F665N F673N F689M F763M F775W F814W F845M F953N
11557	GRW70	F475W
		F200LPF218W F225W F275W F280N F300X F336W F343N F350LPF373N F390M F390W F395N F410M F438W F467M F469N F475W F475X F487N F502N F547M F555W F600LP F606W F621M F625W F631N F645N F656N F657N F658N F665N F673N F680N F689M F763M F775W F814W F845M F850LPF953N
11903	GD153	F225W F275W F336W F350LPF390W F438W F467M F469N F475W F502N F547M F555W F606W F775W F814W F850LP
	GD71	F350LPF390W F438W F467M F469N F475W F502N F547M F555W F606W F775W F814W F850LP
	P330E	F200LPF218W F225W F275W F300X F336W F350LPF390W F410M F438W F467M F475W F475X F547M F555W F600LPF606W F621M F625W F689M F775W F814W F850LP
11907	GRW70	F218W F225W F275W F336W F390M F390W F438W F475W F547M F606W F814W
12333	GRW70	F218W F225W F275W F300X F336W F390M F390W F438W F467M F469N F475W F502N F547M F555W F606W F814W F850LP
12698	GRW70	F218W F225W F275W F300X F336W F390M F390W F438W F467M F475W F502N F547M F555W F606W F814W F850LP
13088	GRW70	F218W F225W F275W F336W F438W F606W F814W
		F200LPF218W F225W F275W F280N F300X F336W F343N F350LPF373N F390M F390W F395N F410M F438W F467M F469N F475W F475X F487N F502N F547M F555W F600LP F606W F621M F625W F631N F645N F656N F657N F658N F665N F673N F680N F689M sF763MF775W F814W F845M F850LPF953N
13089		F200LPF218W F225W F275W F280N F300X F336W F343N F350LPF373N F390M F390W F395N F410M F438W F467M F469N F475W F475X F487N F502N F547M F555W F600LP F606W F621M F625W F631N F645N F656N F657N F658N F665N F673N F680N F689M F763M F775W F814W F845M F850LPF953N
13574	GRW70	F218W F225W F275W F336W F438W F606W F814W
		F200LPF218W F225W F275W F280N F300X F336W F343N F350LPF373N F390M F390W F395N F410M F438W F467M F469N F475W F475X F487N F502N F547M F555W F600LP F606W F621M F625W F631N F645N F656N F657N F658N F665N F673N F680N F689M F763M F775W F814W F845M F850LPF953N
13575		F200LPF218W F225W F275W F280N F300X F336W F343N F350LPF373N F390M F390W F395N F410M F438W F467M F469N F475W F475X F487N F502N F547M F555W F600LP F606W F621M F625W F631N F645N F656N F657N F658N F665N F673N F680N F689M F763M F775W F814W F845M F850LPF953N
13711	G191B2B	F275W F336W F475W F625W F775W
	GD153	F275W F336W F475W F625W F775W
	GD71	F275W F336W F475W F625W F775W
		F200LPF218W F225W F275W F300X F336W F350LPF390M F390W F410M F438W F467M F475W F475X F547M F555W F600LPF606W F621M F625W F689M F763M F775W F814W F845M F850LP
14018	G191B2B	F475W F475X F547M F555W F600LPF606W F621M F625W F689M F763M F775W F814W F845M F850LP
	GRW70	F218W F225W F275W F300X F336W F390M F390W F410M F438W F467M F475W F547M F555W F606W F814W F850LP
14021	GD153	F218W F225W F275W F336W F350LPF438W F475W F547M F555W F600LPF606W F621M F625W F775W F814W F845M

	P330E	F275W F336W F350LPF438W F475W F547M F555W F600LPF606W F621M F625W F775W F814W F845M F850LP
14384	G191B2B	F218W F225W F275W F336W F438W F475W F547M F555W F600LPF606W F621M F625W F775W F814W F845M
	GD153	F218W F225W F275W F336W F350LPF438W F475W F547M F555W F600LPF606W F621M F625W F775W F814W F845M
	GD71	F218W F225W F275W F336W F350LPF438W F475W F547M F555W F600LPF606W F621M F625W F775W F814W F845M
	P330E	F275W F336W F350LPF438W F475W F547M F555W F600LPF606W F621M F625W F775W F814W F845M F850LP
14815	GD153	F218W F225W F275W F336W F438W F606W F814W
	GRW70	F218W F225W F275W F336W F438W F606W F814W
14883	G191B2B	F218W F225W F275W F336W F438W F475W F547M F555W F600LPF606W F621M F625W F775W F814W F845M
	GD153	F218W F225W F275W F336W F350LPF438W F475W F547M F555W F600LPF606W F621M F625W F775W F814W F845M
	GD71	F218W F225W F275W F336W F350LPF438W F475W F547M F555W F600LPF606W F621M F625W F775W F814W F845M
	P330E	F275W F336W F350LPF438W F475W F547M F555W F600LPF606W F621M F625W F775W F814W F845M F850LP
14992	G191B2B	F218W F225W F275W F336W F438W F475W F547M F555W F606W F621M F625W F657N F775W F814W F953N
	GD153	F218W F225W F275W F336W F350LPF438W F475W F547M F555W F600LPF606W F621M F625W F657N F775W F814W F845M
	GD71	F218W F225W F275W F336W F438W F475W F547M F555W F606W F621M F625W F657N F775W F814W F953N
	P330E	F275W F336W F350LPF438W F475W F547M F555W F600LPF606W F621M F625W F775W F814W F845M F850LP
15113	G191B2B	F275W F336W F475W F625W F775W
	GD153	F275W F336W F475W F625W F775W
	GD71	F275W F336W F475W F625W F775W
15398	GD153	F218W F225W F275W F336W F438W F606W F814W
	GRW70	F218W F225W F275W F336W F438W F606W F814W
15399	GD153	F218W F225W F275W F336W F606W F814W
	P330E	F218W F225W F275W F336W F606W F814W
15582	GD153	F218W F225W F275W F336W F438W F475W F547M F555W F606W F621M F625W F657N F775W F814W F845M
	GD71	F218W F225W F275W F336W F438W F475W F547M F555W F606W F621M F625W F657N F775W F814W F953N
	P330E	F275W F336W F350LPF438W F475W F547M F555W F600LPF606W F621M F625W F775W F814W F845M F850LP
	GRW70	F218W F225W F275W F336W F438W F475W F547M F555W F606W F621M F625W F657N F775W F814W F953N
15583	GD153	F218W F225W F275W F336W F438W F606W F814W
	GRW70	F218W F225W F275W F336W F438W F606W F814W

Images were processed with the WFC3 calibration pipeline *calwf3_v3.3* and the latest image photometry table (IMPHTTAB) available in November 2019, *1681905hi_imp.fits*, which corresponds to the 2017 photometric calibration (DE17). The processed charge transfer efficiency (CTE) corrected images, FLC, were multiplied by the pixel area map (PAM, Kalirai et al. 2010) to correct for differences in the area of each pixel on the sky due to the geometric distortion of the

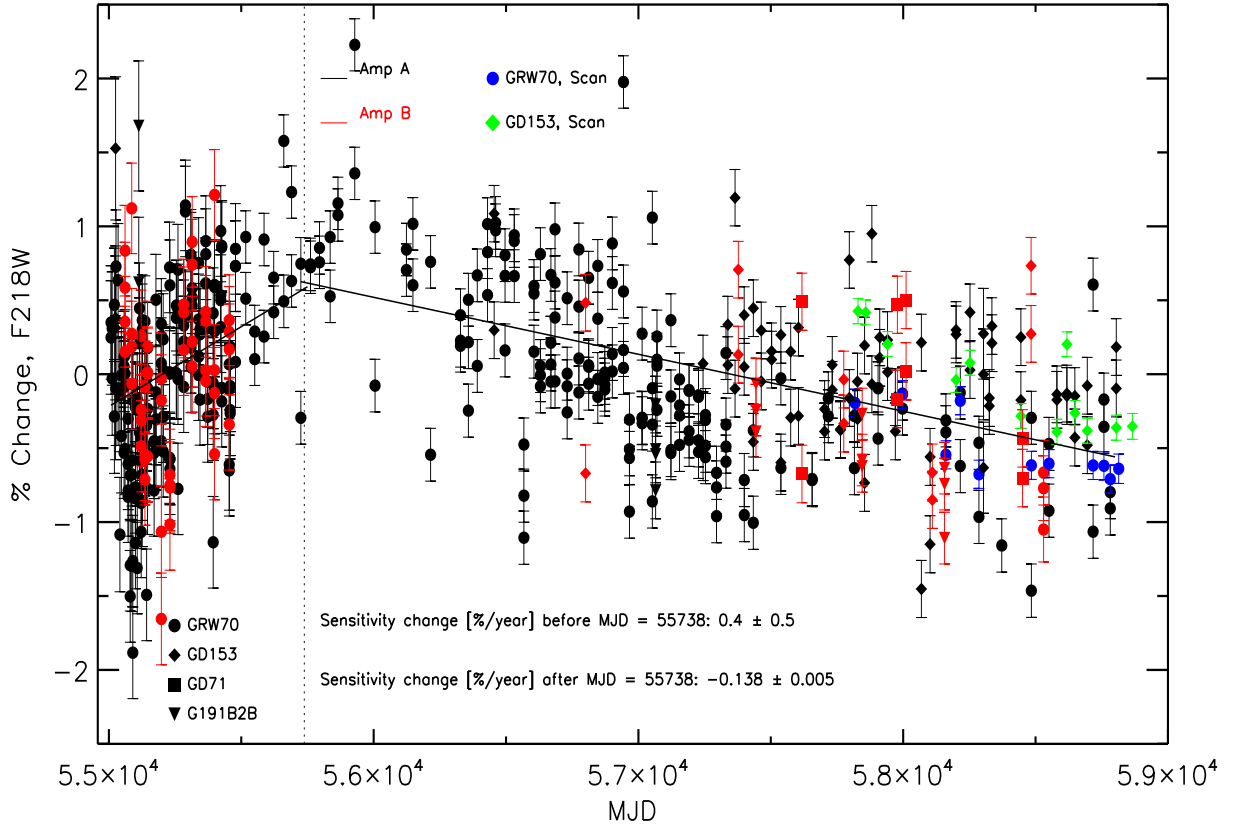


Figure 1: Aperture photometry performed with a 10-pixel radius on FLC images collected in the F218W filter and with the UVIS1-C512A-SUB (Amp A, black) and UVIS1-C512B-SUB (Amp B, red) sub-arrays for five CALSPEC standards, the white dwarfs GRW70 (filled circle), GD153 (diamond), GD71 (square), and G191B2B (triangle), and the G-type star P330E (horizontal triangle) versus the MJD time of observation. Photometry performed on scan images in the same filter and for GRW70 (blue) and GD153 (green) is also shown. The solid lines show the fit to the photometry of all the stars before and after **MJD = 55738**, indicated by a vertical dotted line. The sensitivity change rates in %/yr derived from fitting the data are labeled in the figure.

UVIS1 and UVIS2 detectors.

A `Python` pipeline based on `Photutils` and `WFC3 tools`³ was developed to perform photometry on the thousands of images available. Here we provide a description of the steps followed by the pipeline in order to produce photometric catalogs for each source, image, and filter:

a) Source detection - A first attempt to detect the standard star near the center of the sub-array is made by using a segmentation map: the image is smoothed with a 3×3 pixel kernel with a Full Width Half Maximum (FWHM) of 1.8 pixels. A detection threshold of 30 and 100 connected pixels were found to work for all of the standard star data to find most sources on the first try. If no sources are found on the first try, the detection parameters are adjusted, i.e. threshold is set to 15 and connection pixels to 75, and the segmentation map is created again. If the second try fails, the

³https://github.com/cshanahan1/WFC3-phot_tools/blob/master/WFC3-phot_tools/staring_mode/

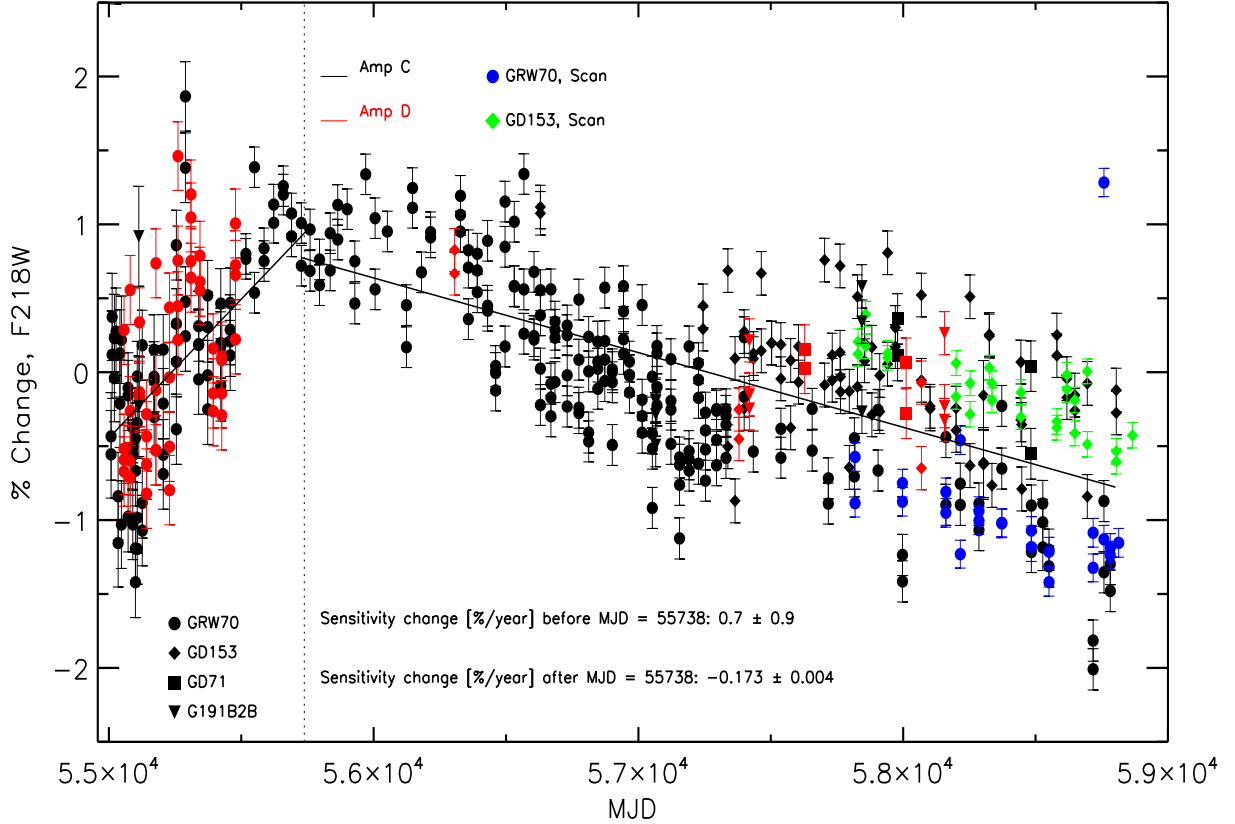


Figure 2: Same as Fig. 1 but for data collected with the UVIS2-C512C-SUB (Amp C, black) and the UVIS2-C512D-SUB (Amp D, red) sub-arrays.

image is discarded; however, this happens in a very small fraction of data, $\leq 2\%$. In the case that two or more sources are found, a method was devised to determine which of those is the correct source, i.e. the standard star. The header keywords *RA_TARG* and *DEC_TARG* are compared to the coordinates of the detected sources, *RA* and *DEC*. Since the proper motion information was not included in the calibration proposals for pre-2015 data, *astroquery* is used to query SIMBAD for the proper motion of the standard stars and these are applied to the *RA_TARG* and *DEC_TARG*. The detected source with coordinates closest to the target location is selected as the correct one;

b) Each FLC image is divided by the exposure time to convert units to e^-/s (count rate);

c) The sky background and sky root mean square (RMS) are calculated as the sigma-clipped mean of the pixels in a circular annulus of 9 pixels with an inner radius of 156 pixels. The sky background is then subtracted from the data;

d) Aperture photometry is measured at different aperture radii, from 1 to 50 pixels;

e) Photometric errors are computed by following the prescription of DAOPHOTIV (Stetson 1987);

f) Count rate outliers that are more than 5% away from the median count rate value on the FLC exposures are clipped before the catalogs are finalized. This cleaning enables the removing of cosmic ray (CR) hits on the source Point-Spread Function (PSF) or of poor measurements.

2.1 Scanned photometry

WFC3 spatial scan observations for two of the four WDs, namely GRW70 and GD153, were also included in the analysis to measure the sensitivity change of the UVIS1 and UVIS2 detectors with time. Spatial scans of bright sources, when compared to staring mode observations, are expected to yield higher precision photometry. Scans allow the collection of millions of source photons without causing saturation by spreading them across many pixels on the detector, and, thereby, reducing the Poisson noise. Averaging over a large number of pixels also helps to reduce noise originating from spatial effects such as bad pixels and flat-field errors. Indeed, it has been determined that sub-0.1% photometric repeatability is possible with spatial scans (Shanahan et al. 2017b).

Table 2: Program number of the regular calibration proposals, standard star name and filter for the spatial scan observations included in this analysis.

Program	Star	Filters							
14878	GRW70	F218W	F225W	F275W	F336W	F438W	F606W	F814W	
	GD153	F218W	F225W	F275W	F336W	F438W	F606W	F814W	
15398	GRW70	F218W	F225W	F275W	F336W	F438W	F606W	F814W	
	GD153	F218W	F225W	F275W	F336W	F438W	F606W	F814W	
15583	GRW70	F218W	F225W	F275W	F336W	F438W	F606W	F814W	
	GD153	F218W	F225W	F275W	F336W	F438W	F606W	F814W	

Spatial scan data were collected during four calibration proposals between 2017 – 2020; Table 2 lists the program numbers, the standard star names and the filters of the scan observations used in this analysis. Program 14878 was exploratory and examined the viability of using spatial scans as a high-precision technique for studying temporal photometric stability. An optimal observation strategy, based on the results from this program, was established by Shanahan et al. (2017b) and all the observations included in this work were obtained following their prescriptions. The data were acquired using either the UVIS1-C512A-SUB (near amplifier A on UVIS1) or the UVIS2-C512C-SUB (near amplifier C on UVIS2) sub-array. In all cases, the single-lined, vertical scan was placed in the middle of the 512 x 512 pixel sub-array.

As in the staring mode data reduction process described above, raw scan images are calibrated using the *calwf3_v3.3* pipeline through the appropriate reduction steps, such as bias correction, dark subtraction, flat-fielding and gain conversion. However, unlike the staring mode data, scan images are not corrected for the CTE effects since these are minimal in the bright spatial scan trails centered within sub-arrays close to the readout amplifiers.

The FLT image products of the pipeline are then further processed by a multi-step reduction routine introduced and described fully in Shanahan et al. (2017b). In summary, this Python based pipeline utilizes various tools from scientific data analysis packages such as *astropy*, *Photutils*, and *WFC3_tools* and performs the following steps:

a) CR detection and repair - Longer exposure times and the spreading of source flux over a large area on the detector make the spatial scans more susceptible to CR hits compared to the staring mode observations. Building on a routine originally developed for CR identification in STIS CCD images, this step identifies CR events in the data. The affected pixels are then repaired by interpolating from unaffected neighboring pixels;

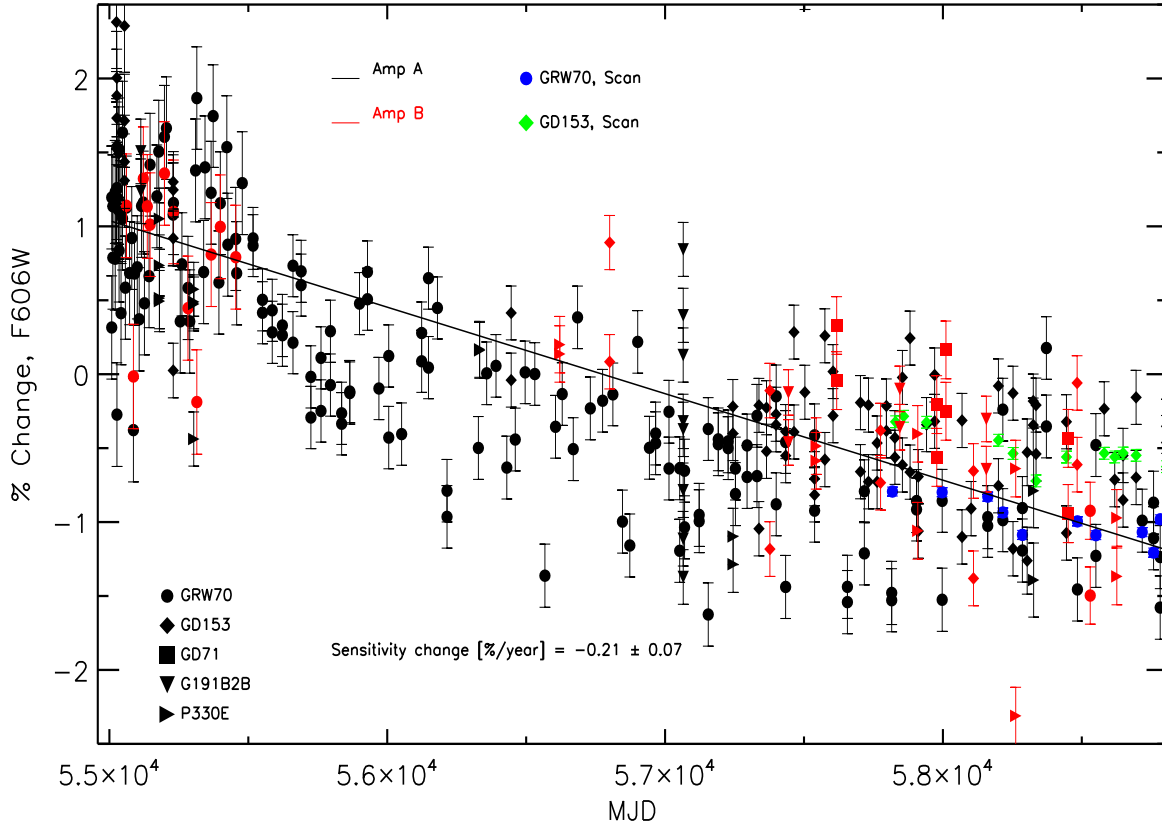


Figure 3: Aperture photometry performed with a 10-pixel radius on FLC images collected in the F606W filter and with the UVIS1-C512A-SUB (Amp A, black) and UVIS1-C512B-SUB (Amp B, red) sub-arrays for five CALSPEC standards, the white dwarfs GRW70 (filled circle), GD153 (diamond), GD71 (square), G191B2B (triangle), and the G-type star P330E (horizontal triangle) versus the MJD time of observation. Photometry performed on scan images in the same filter and for GRW70 (blue) and GD153 (green) is also shown. The solid line shows the fit to the photometry of all the stars. The sensitivity change rate is labeled in the figure.

d) Determining scan location - Each image is designed to have the single-lined, vertical scan positioned at the center of the sub-array. However, to account for small shifts, an automated determination of the scan centroid location is performed for each image. A simultaneous determination of the scan direction is also performed. However, as mentioned before, the entire dataset considered in this work comprises of vertical scans only;

c) Sky background subtraction - The sky region corresponding to each vertical scan is defined as all pixels excluding a 10-pixel wide strip bordering the sub-array and a 350 x 75 pixel rectangular region centered on the scan. The sky background level and the sky RMS are calculated as the sigma-clipped mean and RMS of all the sky pixels. This background is then subtracted from the data and the errors are propagated accordingly;

c) Scaling with pixel area maps - The sky subtracted image is scaled by applying the appropriate PAM to account for geometric distortions of the detector;

d) Aperture photometry - The last step in this process is to perform aperture photometry on

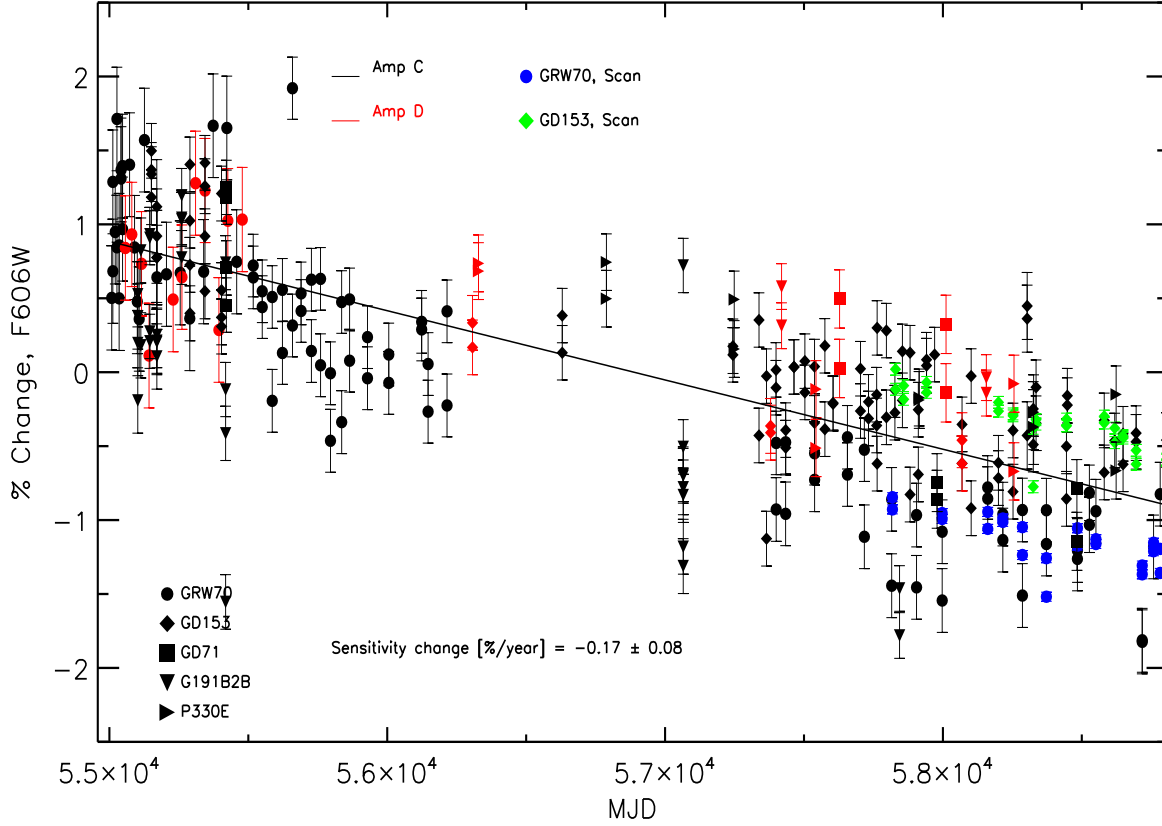


Figure 4: Same as Fig. 3 but for data collected with the UVIS2-C512C-SUB (Amp C, black) and the UVIS2-C512D-SUB (Amp D, red) sub-arrays.

the sky-subtracted, PAM corrected image to determine the sum of pixels in the scan. This is done using a 240×36 pixel rectangular aperture placed at the scan centroid determined in step *b*). The dimensions of the aperture were chosen such that it is large enough to contain the scan in its entirety, yet it is not too large to be affected by noise from the sky subtraction. In this regime of very high total source counts, the Poisson noise term should dominate and is therefore approximated as the measurement error. Finally, the photometric measurement is converted into source count-rate (e^-/s) by dividing the sum of pixels by the image exposure time.

This pipeline was written in `Python` and is available on a Github repository.⁴

3 Data Analysis

Aperture photometry with a 10-pixel radius for each standard star and filter is normalized to their mean value over the full time interval and the percent change of the count rates is plotted as a function of MJD of observation. The spatial scan photometry for GRW70 and GD153, when available, is normalized to the staring mode photometry at 10 pixel for the same stars in the same time interval, $\sim 55700 - 58800$, i.e. $\sim 2016.8 - 2019.8$, and values are overplotted. As shown in

⁴https://github.com/cshanahan1/WFC3_phot_tools/blob/master/WFC3_phot_tools/spatial_scan/

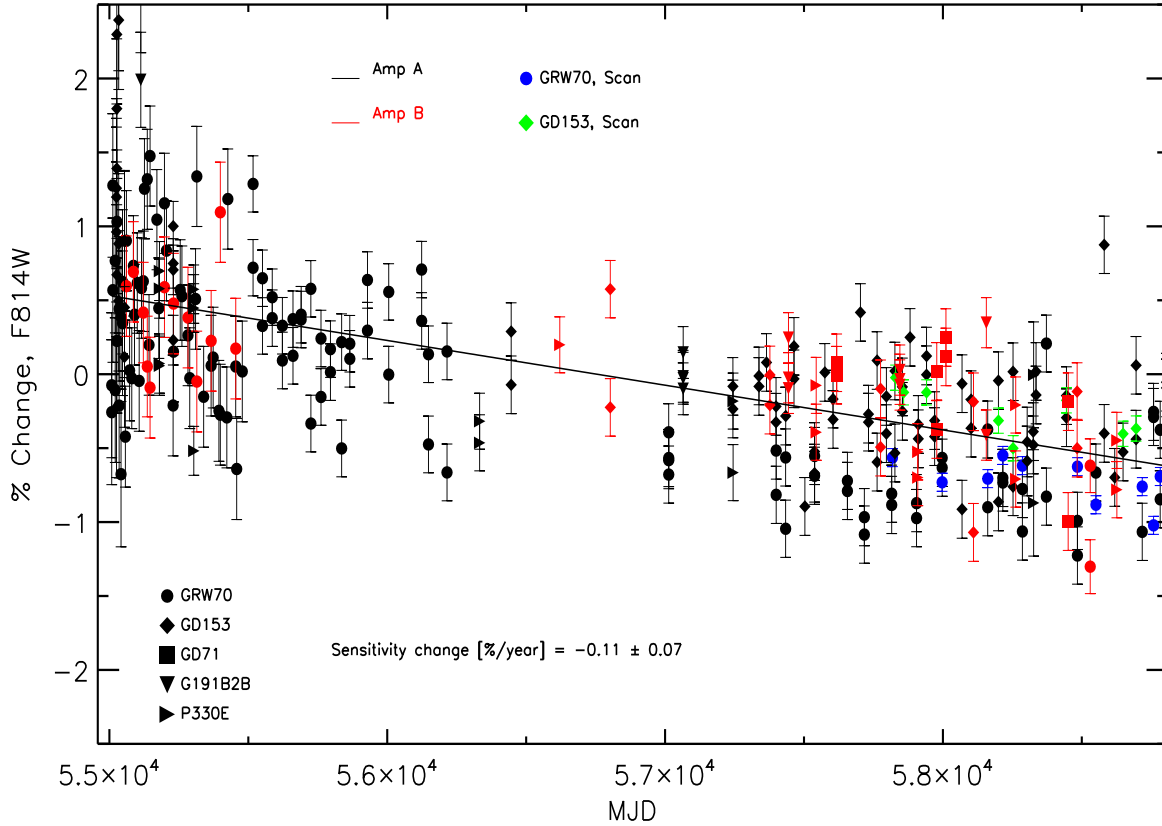


Figure 5: Same as Fig. 3 but for the $F814W$ filter.

Figs. 1, 2, 3, 4, 5, and 6, a small offset between the percent change of the photometry of different standard stars is present. However, we only use these plotted data to determine the best sensitivity change slopes and then use the single standard star observations to determine the final normalized photometry for each target in all filters. The WFC3-UVIS detectors are divided in two amplifiers, Amp A and B (UVIS1) and Amp C and D (UVIS2, a map of the WFC3-UVIS detector and its amplifiers can be found in the Data Handbook, Section 1.2⁵); since most measurements of the standard stars were collected on Amp A and Amp C, photometry on Amp B and D is normalized to photometry on Amp A and C, respectively, to correct for small ($\lesssim 1\%$) errors in the flat field across the detector.

Plots of the time-dependent sensitivity evolution are displayed for filters $F218W$, $F606W$, and $F814W$ in Figs. 1, 2, 3, 4, 5, 6, respectively. Figs. 1 and 2 show that in the case of the $F218W$ filter, the sensitivity of the UVIS detector increases with time for the first 2 years (from MJD = 55008 to ~ 55738) of WFC3 life and later decreases. The same happens for the other ultraviolet (UV) filters ($F225W$, $F275W$ and $F280N$). This effect was already observed in Shahanan et al. (2017a) and Khandrika et al. (2018) and it is also present in other instruments with UV capabilities on board HST, such as STIS (Carlberg et al. 2017).

In order to calculate the sensitivity changes over time we perform a first least-square linear fit

⁵<https://hst-docs.stsci.edu/wfc3dnhb/chapter-1-wfc3-instruments/1-2-the-uv-vis-channel>

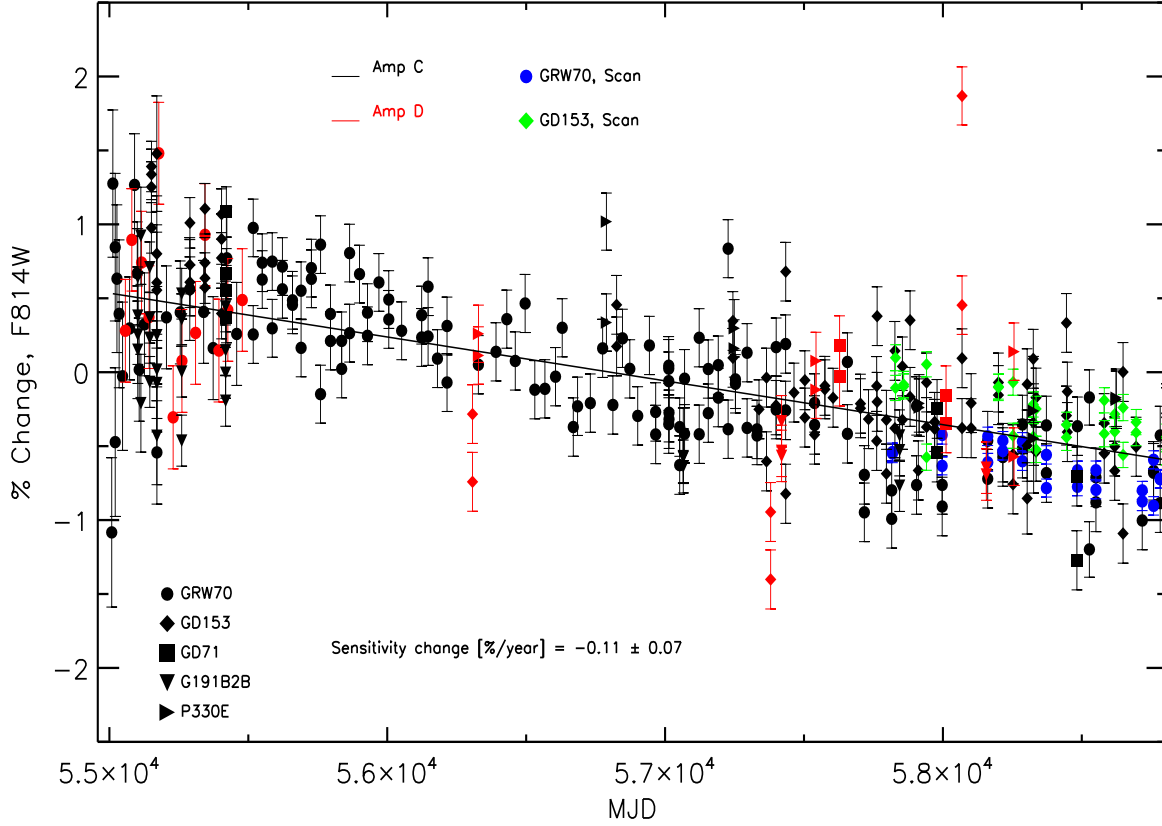


Figure 6: Same as Fig. 5 but for data collected with the UVIS2-C512C-SUB (Amp C, black) and the UVIS2-C512D-SUB (Amp D, red) sub-arrays.

by including all the measurements from the five standard stars. In the case of the UV filters, we perform two different fits, one for $MJD \leq 55738$ and a second for all data acquired through $MJD \approx 58800$, to take into account the change from an increase to a decrease of the sensitivity. We then apply a 2.5σ clip of the outlier measurements and perform a second least-square fit that results in the final slopes values. These are indicated as Sensitivity change rates (%/year) in Figs. 1, 2, 3, 4, 5, 6. The final slopes values with their uncertainties for UVIS1 and UVIS2 are listed in Table 3 and are plotted as a function of the filter pivot wavelength in Figs. 7 and 8.

In the case of some filters, mostly narrow- or medium-band or long pass, there are not enough photometric measurements to allow a slope to be calculated. Therefore, we assume that the sensitivity change rates of these filters are the same of filters very close in wavelength. For example, the slope for filter *F373N* (pivot wavelength 3730 \AA) is assumed to be the same as for *F390M* (pivot wavelength 3897 \AA , see Table 3).

Once all the slopes are finalized, we use them to normalize the 10-pixel radius aperture photometry for each standard star and filter to the reference epoch $MJD = 55008$ (June 26, 2009), corresponding to the time at which the first WFC3 observations were being collected. A weighted mean of all measurements is then calculated after a 2.5σ -clipping of the outliers. The mean is then used to define the value at the reference epoch of the photometry for each standard star at 10 pixels in units of count/s, i.e. count rates. The same slopes will be also used to derive six different

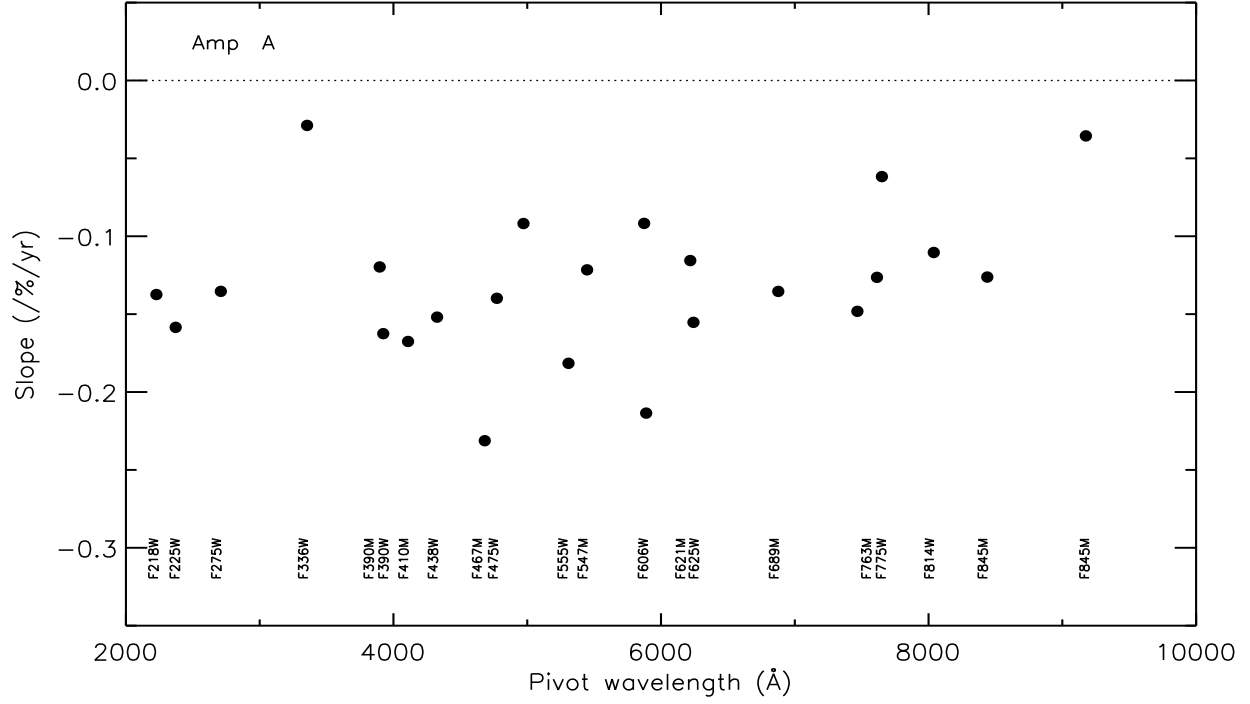


Figure 7: Measured sensitivity change slopes for the wide- and medium-band filters for the UVIS1 detector (Amp A) as a function of pivot wavelength. Note that for the three UV filters the slope is the one calculated after MJD = 55738 (see text and Table 3 for more details).

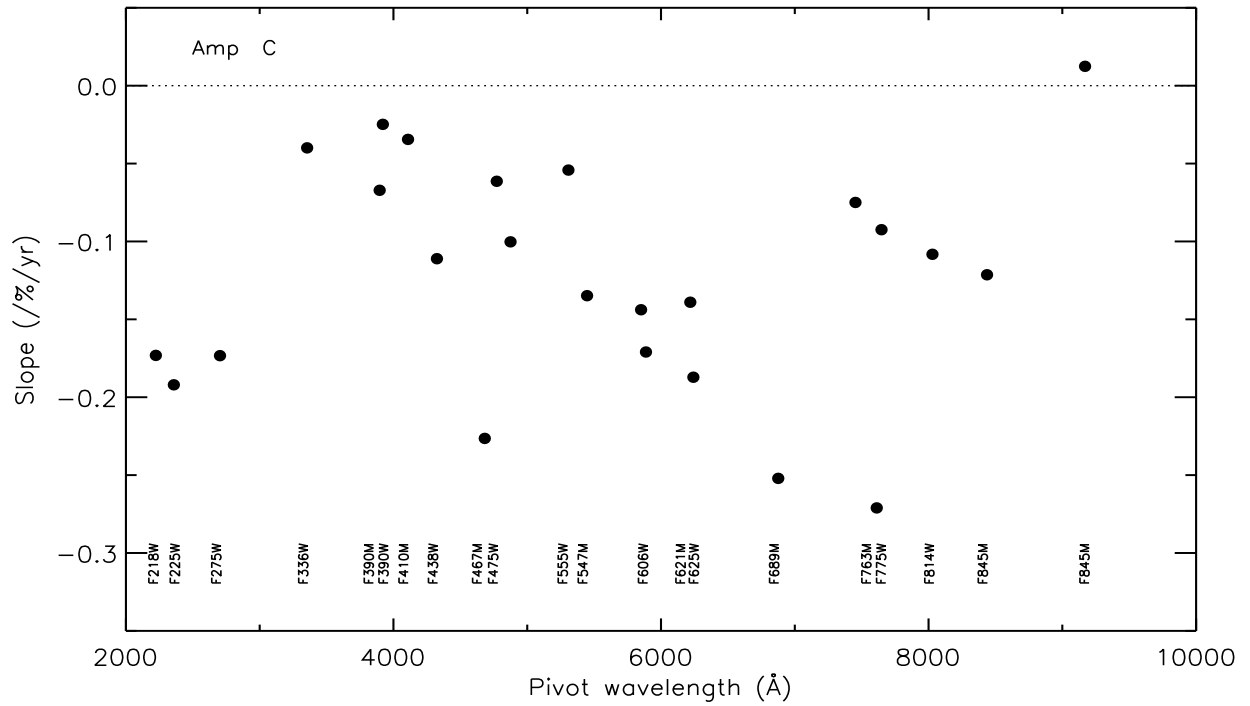


Figure 8: Same as Fig. 7 but for the UVIS2 detector (Amp C).

Table 3: Slopes and their $1-\sigma$ dispersion of the sensitivity changes for UVIS1 (Amp A) and UVIS2 (Amp C) 42 full-frame filters. The UV filters have two slopes, one for $MJD \leq 55738$ and one for later times, while the redder filters have only one slope (see text for more details).

Filter	Pivot (Å)	Slope1/ σ ($MJD \leq 55738$) (%/yr)	Slope2/ σ ($MJD > 55738$) (%/yr)	Pivot	Slope1/ σ ($MJD \leq 55738$) (%/yr)	Slope2/ σ ($MJD > 55738$) (%/yr)
UVIS1 (Amp A)				UVIS2 (Amp C)		
F200LP	4971.86	...	-0.092/0.674	4875.10	...	-0.100/2.057
F218W	2228.04	0.394/0.532	-0.137/0.006	2223.72	0.685/0.863	-0.173/0.004
F225W	2372.05	0.228/0.479	-0.158/0.005	2358.39	0.552/0.790	-0.192/0.003
F275W	2709.69	0.120/0.564	-0.135/0.005	2703.30	0.337/0.806	-0.173/0.004
F280N	2832.86	0.023/0.627	-0.138/0.007	2829.98	0.337/0.806	-0.173/0.004
F300X	2820.47	0.023/0.627	-0.138/0.007	2805.84	...	-0.040/0.068
F336W	3354.49	...	-0.029/0.075	3354.66	...	-0.040/0.068
F343N	3435.15	...	-0.029/0.080	3435.19	...	-0.049/0.076
F350LP	5873.87	...	-0.092/0.199	5851.15	...	-0.144/0.479
F373N	3730.17	...	-0.120/0.269	3730.17	...	-0.067/0.287
F390M	3897.24	...	-0.120/0.269	3897.00	...	-0.067/0.287
F390W	3923.69	...	-0.162/0.295	3920.72	...	-0.025/0.017
F395N	3955.19	...	-0.053/0.950	3955.15	...	-0.025/0.017
F410M	4108.99	...	-0.167/0.318	4108.88	...	-0.034/0.357
F438W	4326.23	...	-0.152/0.063	4325.14	...	-0.111/0.074
F467M	4682.58	...	-0.231/0.277	4682.60	...	-0.226/0.289
F469N	4688.10	...	-0.048/0.492	4688.10	...	-0.180/0.317
F475W	4773.10	...	-0.140/0.134	4772.17	...	-0.061/0.099
F475X	4940.72	...	-0.133/0.474	4937.41	...	-0.192/0.893
F487N	4871.38	...	-0.116/0.446	4871.38	...	-0.061/0.099
F502N	5009.64	...	-0.123/0.422	5009.64	...	-0.133/0.322
F547M	5447.50	...	-0.121/0.128	5447.24	...	-0.135/0.133
F555W	5308.43	...	-0.181/0.154	5307.91	...	-0.054/0.207
F600LP	7468.12	...	-0.148/0.185	7453.66	...	-0.075/0.339
F606W	5889.17	...	-0.213/0.068	5887.71	...	-0.171/0.075
F621M	6218.85	...	-0.116/0.155	6219.16	...	-0.139/0.220
F625W	6242.56	...	-0.155/0.169	6241.96	...	-0.187/0.191
F631N	6304.29	...	-0.000/1.903	6304.28	...	0.000/1.533
F645N	6453.59	...	-0.000/1.903	6453.58	...	-0.001/1.534
F656N	6561.37	...	-0.031/0.373	6561.36	...	-0.023/0.301
F657N	6566.63	...	-0.031/0.373	6566.60	...	-0.023/0.301
F658N	6584.02	...	-0.031/0.373	6583.92	...	-0.012/1.322
F665N	6655.88	...	-0.031/0.373	6655.84	...	0.000/1.525
F673N	6765.94	...	-0.031/0.373	6765.91	...	0.000/1.525
F680N	6877.60	...	-0.135/0.476	6877.41	...	-0.000/4.050
F689M	6876.75	...	-0.135/0.476	6876.50	...	-0.252/0.581
F763M	7614.37	...	-0.126/0.470	7612.74	...	-0.271/0.545
F775W	7651.36	...	-0.062/0.162	7648.30	...	-0.092/0.158
F814W	8039.06	...	-0.110/0.066	8029.32	...	-0.108/0.072
F845M	8439.06	...	-0.126/0.197	8437.27	...	-0.121/0.173
F850LP	9176.13	...	-0.035/0.147	9169.94	...	0.012/0.181
F953N	9530.58	...	-0.016/0.090	9530.50	...	-0.016/0.090

inverse sensitivity values as a function of time (MJD) to enable the *calwf3* pipeline to determine inverse sensitivities at different observing epochs by interpolating over these points (more details will be provided in the following sections). Therefore, the fact that the two least-square fit lines in the case of the *F218W* filter (Figs.1 and 2) do not perfectly coincide at the established inversion epoch, $MJD = 55738$, does not affect the inverse sensitivity calculation.

4 Encircled energy corrections

In order to calculate new inverse sensitivities at *infinity*, where *infinity* indicates the radius that should enclose all the light emitted by the target, we first need to derive encircled energy (EE) corrections to be applied to the 10-pixel aperture photometry of the standard stars. We now have the sensitivity change slopes for all filters and both detectors, and we can apply these corrections to the science array of each individual image of a standard star prior to combine them with `AstroDrizzle` to calculate the EE fractions. This is fundamental since the EE fractions are needed to bring the standard star photometry to *infinity* and uncertainties in the EEs are carried over in the uncertainty of the inverse sensitivities. We tested this new procedure to derive EE corrections for two filters, *F275W* and *F814W*, respectively. *F275W* was selected because the EE values in the DE16 solution differ by $\approx 1\%$ from the original in-flight EE calculation by Hartig (2009). *F814W* was selected because the EE in the DE16 solution for the two detectors differs by $\approx 0.5\%$ or more for the reddest filters (see Fig.11).

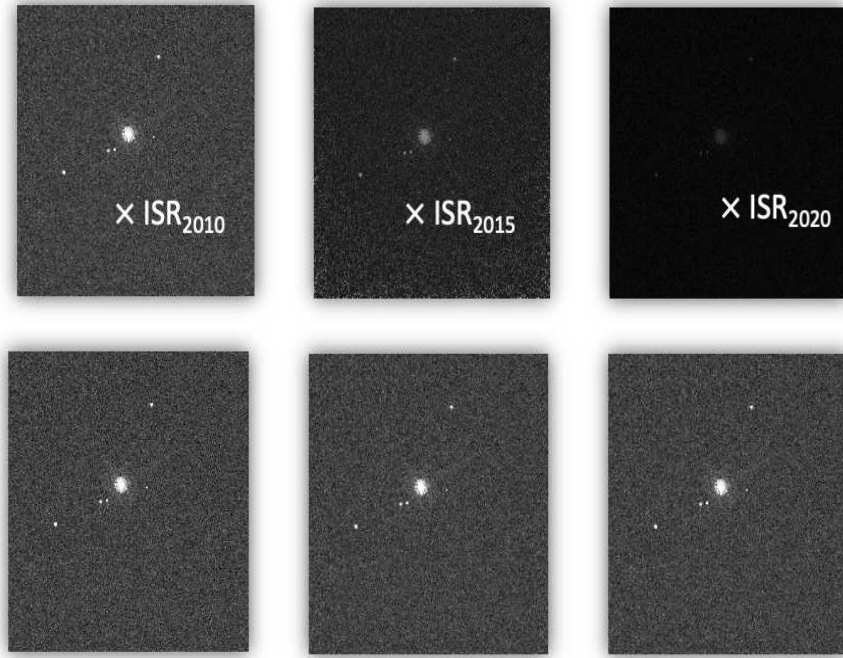


Figure 9: A visual representation of the FLC images (in units of electrons) of GRW70 observed at three different epochs (2010, 2015, and 2020) before (top panels) and after (right) being multiplied by their corresponding inverse sensitivity ratio (ISR). Note that the scale difference between the images is artificially enhanced to better show the time dependent sensitivity changes with time.

EEs are calculated by using all observations collected in *F275W* and *F814W* for the standard star GRW70 from the reference epoch (MJD = 55008) until about MJD = 58800. The new method to derive EE fractions relies on the sensitivity change slopes to scale the FLC image science array pixel values before combining them in a final stacked image (DRC), used to derive the photometry at different aperture radii. EE fractions are then calculated as the ratio of fluxes at different aperture radii and the flux at *infinity*, i.e. the flux at 150 pixels ($\approx 6''$). In particular, each FLC image of GRW70 is multiplied by a inverse sensitivity ratio, that is the image time-dependent inverse

sensitivity value divided by the value at the reference epoch. This process removes the time-dependence from the FLC images as shown in Fig. 9, a visual representation of how the inverse sensitivity ratio scales FLC images observed at three different epochs.

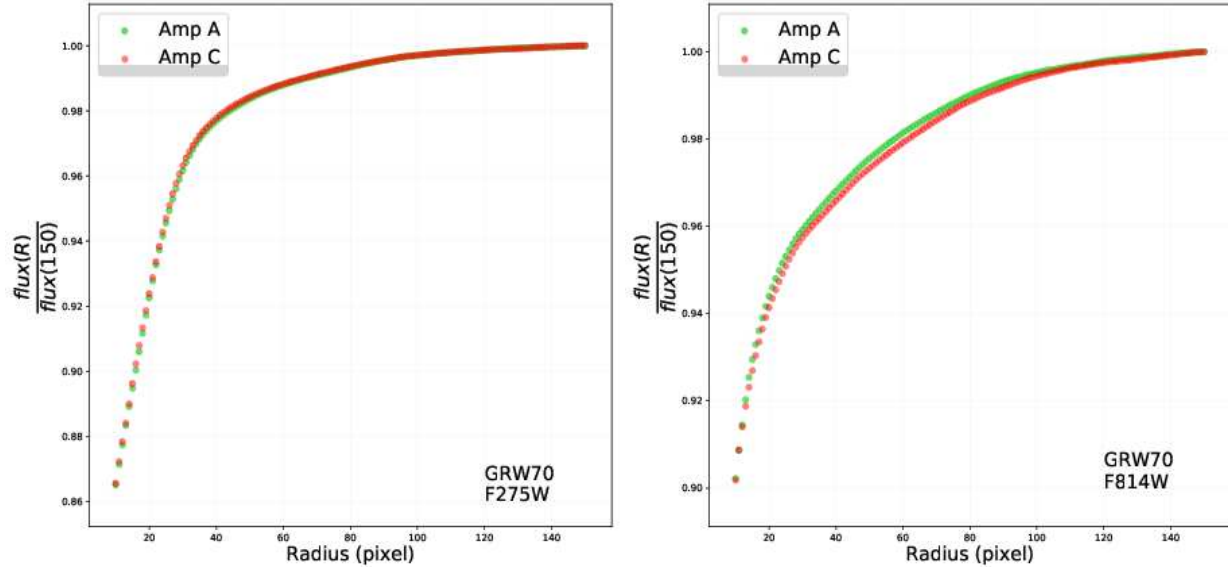


Figure 10: Encircled energy fraction, $flux(R)/flux(150)$, as a function of the aperture radius in pixels, R , for Amp A (UVIS1, green circles) and Amp C (UVIS2, red) for the $F275W$ (left panel) and the $F814W$ filter (right). Photometry was measured on the combined (DRC) images for the standard star GRW70. See text for more details.

The FLC images⁶ are then processed by using the task `phot_eq`⁷ to correct their data values by scaling them with the respective inverse sensitivity ratio; in this way, all FLC images have roughly equal count rates, which is required for optimal image combination with `AstroDrizzle`. The scaled FLC images are then processed through `Astrodrizzle` to create the combined DRC image that will be used for the EE fraction calculation. For both filters, the DRC image is a combination of over 100 individual FLC images, significantly improving the signal-to-noise ratio of the standard star and the background statistics, thus enhancing the visibility of the Point-Spread Function (PSF) wings. This is very important to achieve more precise photometric measurements at larger aperture radii.

Whereas the drizzle algorithm uses pointing information from the FLC image header to align images on the sky, our new approach aligns the images in detector coordinates. This ensures that the drizzled PSF does not rotate as the nominal HST orientation varies over the year, which changes the position of the diffraction spikes and structure in the PSF wings. This is done by modifying the following astrometry header keywords for each FLC image:

- `CRPIX1` and `CRPIX2` are modified to match the X,Y position of the centroid of the star in each image;

⁶The FLC images have also been corrected for distortion using the PAM prior to drizzling

⁷<https://drizzlepac.readthedocs.io/en/latest/photeq.html>

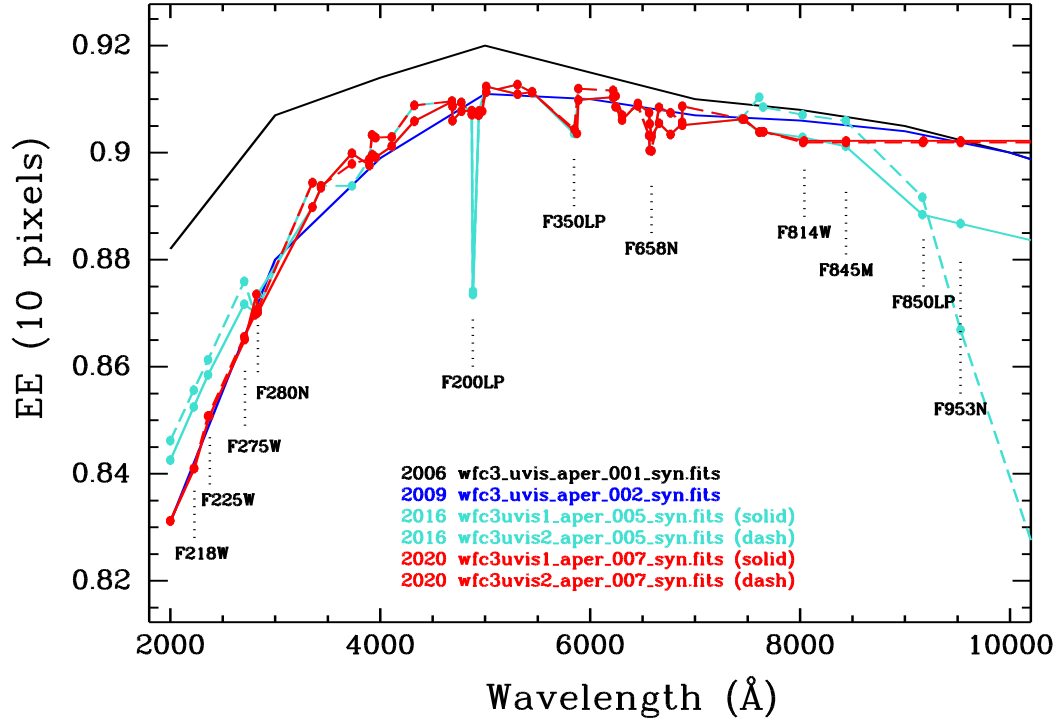


Figure 11: Old (cyan solid and dashed lines) and new (red) EE corrections for the UVIS1 and UVIS2 detectors as a function of wavelength. The EE model values from Hartig (2009) are shown with a blue solid line and the pre-launch values with a black solid line.

- CRVAL1 and CRVAL2 are set to match that of the reference image in order to remove any proper motion applied to the RA and DEC of the standard star over the 10 years;
- The linear terms of the CD matrix (CD1_1, CD1_2, CD2_1, CD2_2) are set to the value in the reference image in order to remove any orientation and plate scale changes with date.

Once the astrometry header keywords are updated, we combine all the FLC images using the non-default `AstroDrizzle` parameter values listed in Table 4. By aligning the star in detector space, we are able to accurately flag and reject artifacts such as cosmic rays, unstable hot pixels, while not affecting any PSF structure, with minimal pixel resampling.

Photometry is performed on the DRC images for both filters for aperture radii in the range 1 –

Table 4: *Astrodriizzle* input parameter names with their description and corresponding values.

Name	Description	Value
skymethod	Equalize sky background between the input frames	match
skystat	Use the sigma-clipped mean background	mean
driz_sep_bits	For single images, set DQ values considered to be <i>good</i> data	80
combine_type	Combine images using the median	median
combinie_nhigh	Set the number of high value pixels to reject for the median combination	1
driz_cr_snr	S/N to be used in detecting CRs, performed in two iterations	3.5 3.0
driz_cr_scale	Scaling factors applied to the derivative for detecting CRs	2.0 1.5
final_bits	For the final image stack, set DQ values considered to be <i>good</i> data,	80

150 (*infinity*) pixels. The sky value used for background subtraction is computed as the σ -clipped mean value in an annulus with radii in the range 160 – 200 pixels.

We find improved agreement in the new EE fraction values between the two detectors for both the $F275W$ and the $F814W$ filters: the fraction of flux included in 10 pixels is $86.51 \pm 0.54\%$ for UVIS1 and $86.56 \pm 0.54\%$ for UVIS2 for $F275W$, as shown in the left panel of Fig. 10, and it is $90.22 \pm 0.59\%$ (UVIS1) and $90.19 \pm 0.58\%$ (UVIS2) for $F814W$, as shown in the right panel of Fig. 10. The new EE fractions for the $F275W$ filter differ by $\approx 1\%$ from the previously calculated EE at 10 pixels from DE16 and DE17, which were 87.20% and 87.59%. In the case of the $F814W$ filter, the value for the UVIS1 detector is in quite good agreement with the previous one, 90.22 vs 90.29%, while differs by $\approx 0.5\%$ for UVIS2, 90.19 vs 90.71%. The new EE corrections agree very well with the EE values from the 2009 optical model (Hartig 2009). The comparison between the new EE fractions at 10 pixels for $F275W$ and $F814W$ and the 2016 and 2009 values is shown in Fig. 11.

Following the results for these two filters, we corrected the EE values for the other UV filters, namely $F218W$, $F225W$, and $F280N$, for both detectors, scaling them by the difference between the new and old $F275W$ values (see solid and dashed red lines and the marked filter names in Fig. 11). In the case of filters with pivot wavelengths longer than $F814W$, namely $F845M$, $F850LP$ and $F953N$ (also marked in Fig. 11), we assumed for them the same EE correction derived for $F814W$ for both detectors. EE corrections from 2016 for a few Long-Pass and narrow-band filters (marked in the figure) are in large disagreement with the 2009 model values; therefore, we assumed as EE fractions for these filters the interpolated EE values of the closest two filters in wavelength.

New aperture correction files were created, *wfc3uvis1_aper_007_syn.fits* and *wfc3uvis2_aper_007_syn.fits*, and are shown as solid and dashed red lines in Fig. 11, while the DE16 correction files, *wfc3uvi1_aper_005_syn.fits* and *wfc3uvi2_aper_005_syn.fits*, are shown as solid and dashed cyan lines, and the 2009 model values, *wfc3_uvis_aper_002_syn.fits*, as a solid blue line. The pre-launch EE values, *wfc3_uvis_aper_001_syn.fits*, are also shown as a black solid line.

5 New in-flight and filter corrections

We use the new EE values to correct the standard star photometry from a 10 pixel aperture radius to *infinity*. We end up with mean count rates for each standard star as observed with the two detectors

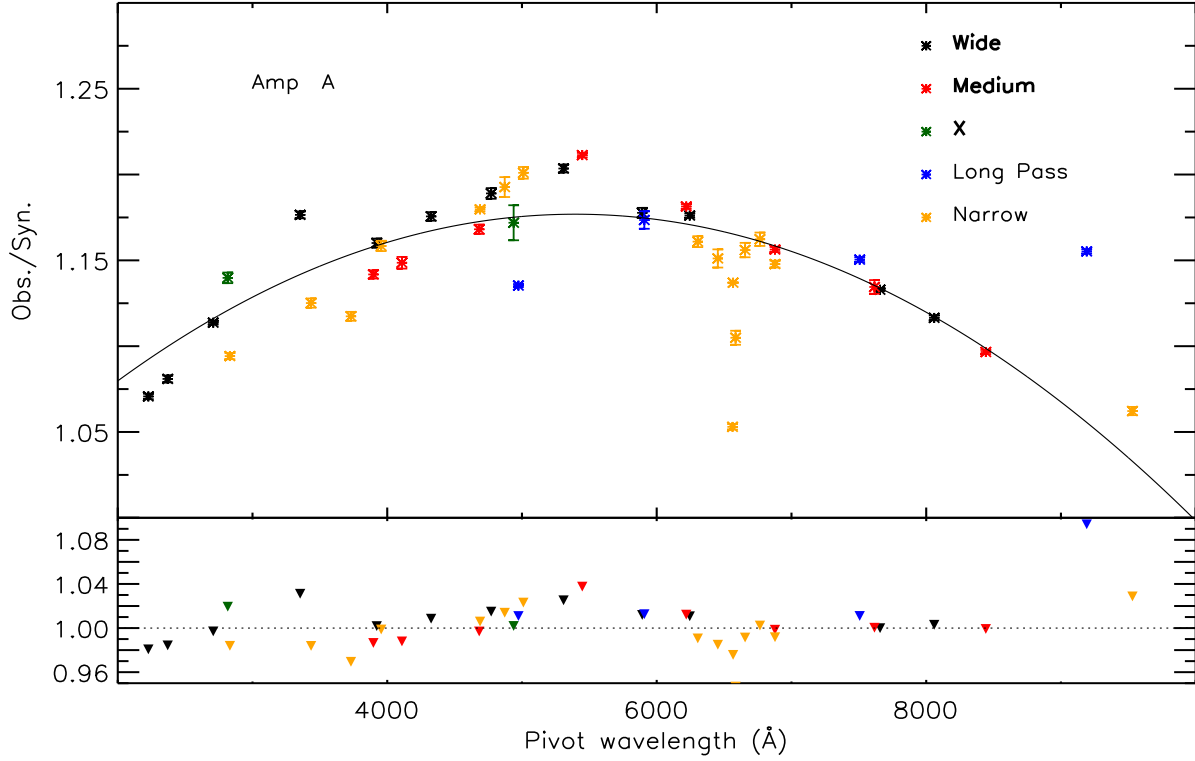


Figure 12: Observed over synthetic count rates for the 42 WFC3 UVIS1 (Amp A) filters: wide (black), medium (red), X (green), Long Pass (blue), and narrow (orange). These were calculated as a weighted mean over the standard stars (see text for more details). Error bars are displayed. The solid black line is a quadratic polynomial least-square fit to the data of the wide, medium and X filters only, and the small triangles are the residual ratios after the fit.

through all the 42 full-frame filters and at the reference epoch MJD = 55008.

We proceed to calculate new in-flight corrections for UVIS1 and UVIS2 by using *Pysynphot*⁸ (Lim et al. 2015) to predict the count rates for each filter and standard star as observed with the two detectors at the reference epoch. In order to do this, we use for the *Pysynphot* simulations the new standard star SEDs (BO20, CALSPECv11), the old in-flight correction files (003), the old filter curves (002/003), and the new aperture correction files (007), all listed in Table 5. We then derive the ratio of observed over synthetic count rates for each star, detector and filter: in the case of UV and bluer filters, i.e. for wavelengths $\lambda < 6000\text{\AA}$, we calculate a weighted mean of the ratios by using the four standard WDs, while for longer wavelengths we use all five stars in the calculations, i.e. we include the G-type star P330E, when measurements are available. We follow this strategy since photometric measurements for P330E have a much lower S/N in the bluer filters and a significant color term (≈ 1 to 8%) is present when observing red sources with UV filters, i.e. the response of the detector and filter for red stars is different compared to the response for blue stars (Calamida et al. 2018). Figs. 12 and 13 show the ratios of observed over synthetic count rates for all filters and Amp A and C, respectively. The ratio values for all filters are larger than 1.0, i.e. the filter throughputs were underestimated before WFC3 launch. A very similar result was found

⁸<https://pysynphot.readthedocs.io/en/latest/>

Table 5: Files used in the synthetic simulations performed with *Pysynphot*.

Component	Description
Simulations to derive the new in-flight correction	
wfc3_uvis_cor_003_syn.fits	Pre-launch correction
wfc3uvis1_aper_007_syn.fits	New aperture correction for UVIS1
wfc3uvis2_aper_007_syn.fits	New aperture correction for UVIS2
wfc3_uvis_FXXXX_002/003_syn.fits	Pre-launch filter curves (TV3)
gd153_stiswfcnic_002.fits	New CALSPEC SED
gd71_stiswfcnic_002.fits	New CALSPEC SED
gd191b2b_stiswfcnic_002.fits	New CALSPEC SED
grw_70d5824_stiswfcnic_002.fits	New CALSPEC SED
p330e_stiswfcnic_002.fits	New CALSPEC SED
Simulations to derive the new filter curves	
wfc3_uvis_cor_005_syn.fits	New in-flight correction
wfc3uvis1_aper_007_syn.fits	New aperture correction for UVIS1
wfc3uvis2_aper_007_syn.fits	New aperture correction for UVIS2
wfc3_uvis_FXXXX_002/003_syn.fits	Pre-launch filter curves (TV3)
gd153_stiswfcnic_002.fits	New CALSPEC SED
gd71_stiswfcnic_002.fits	New CALSPEC SED
gd191b2b_stiswfcnic_002.fits	New CALSPEC SED
grw_70d5824_stiswfcnic_002.fits	New CALSPEC SED
p330e_stiswfcnic_002.fits	New CALSPEC SED
Simulations to derive the final synthetic count rates	
wfc3_uvis_cor_005_syn.fits	New in-flight correction
wfc3uvis1_aper_007_syn.fits	New aperture correction for UVIS1
wfc3uvis2_aper_007_syn.fits	New aperture correction for UVIS2
wfc3uvis1_FXXXX_008_syn.fits	New filter curves for UVIS1
wfc3uvis2_FXXXX_008_syn.fits	New filter curves for UVIS2
gd153_stiswfcnic_002.fits	New CALSPEC SED
gd71_stiswfcnic_002.fits	New CALSPEC SED
gd191b2b_stiswfcnic_002.fits	New CALSPEC SED
grw_70d5824_stiswfcnic_002.fits	New CALSPEC SED
p330e_stiswfcnic_002.fits	New CALSPEC SED

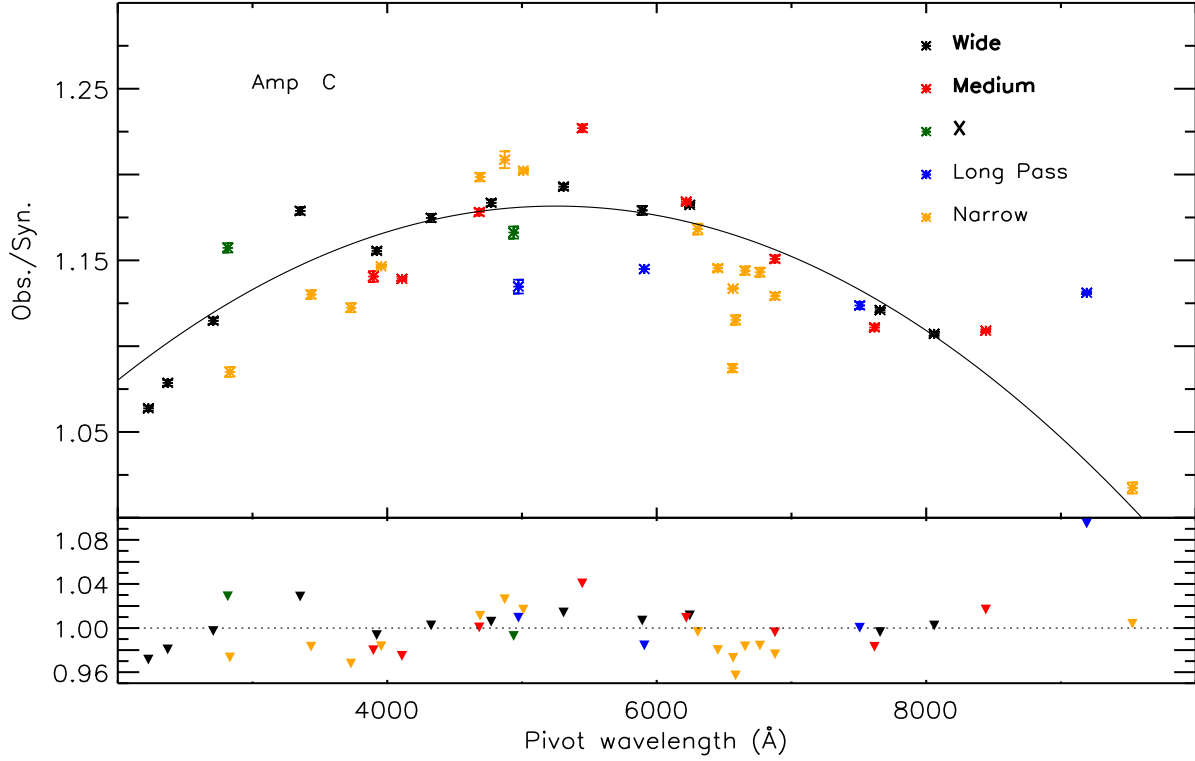


Figure 13: Same as Fig. 12 but for the 42 WFC3 UVIS2 (Amp C) filters.

by Kalirai et al. (2009, see their Fig. 5) and DE16 (see their Fig. 8) based on observations collected in 2009 and 6 years of standard star photometry, respectively. The pre-launch throughput values were measured during TV3 and were systematically underestimated, on average by 5–10% and up to 20% for wavelengths around $\lambda \sim 5000\text{\AA}$. A possible explanation provided by Kalirai et al. is that the TV3 calibration error was due to problems with the *CASTLE* apparatus (see also Brown et al. 2008).

The residuals of the observed over synthetic ratios after applying the new in-flight corrections are larger for the narrow-band filters (see bottom panel in Figs. 12 and 13), as expected, due to the availability of many less standard star measurements in these filters compared to the others, the lower S/N , and in some cases the presence of absorption lines. For example, the ratio and the residual for the *F656N* filter are systematically lower (by ≈ 10 and 5%) compared to the other filters, probably due to the presence of a H_α line in the standard WD SEDs. The long-pass filters also show slightly larger residuals due to few measurements available. Therefore, we only use the wide-, medium-band and the X-wide filters to derive the new in-flight corrections. A least-square fit with a quadratic polynomial resulted the best method to reproduce the data points and it is shown with a solid line in Figs. 12 and 13. The bottom panel of the figures shows the residual ratios for each filter after the fit. The ratios between observed and synthetic count rates have a mean value of 1.00 with a dispersion $\sigma \sim 0.02$.

We then create a new in-flight correction file for each detector, *wfc3uvis1_cor_005_syn.fits* and *wfc3uvis2_cor_005_syn.fits*, by using the derived polynomials (see Table 5). New synthetic count rates were then calculated with the new in-flight corrections, the same SEDs, filter curves and aperture corrections. The ratio of observed and new synthetic count rates was used to derive a

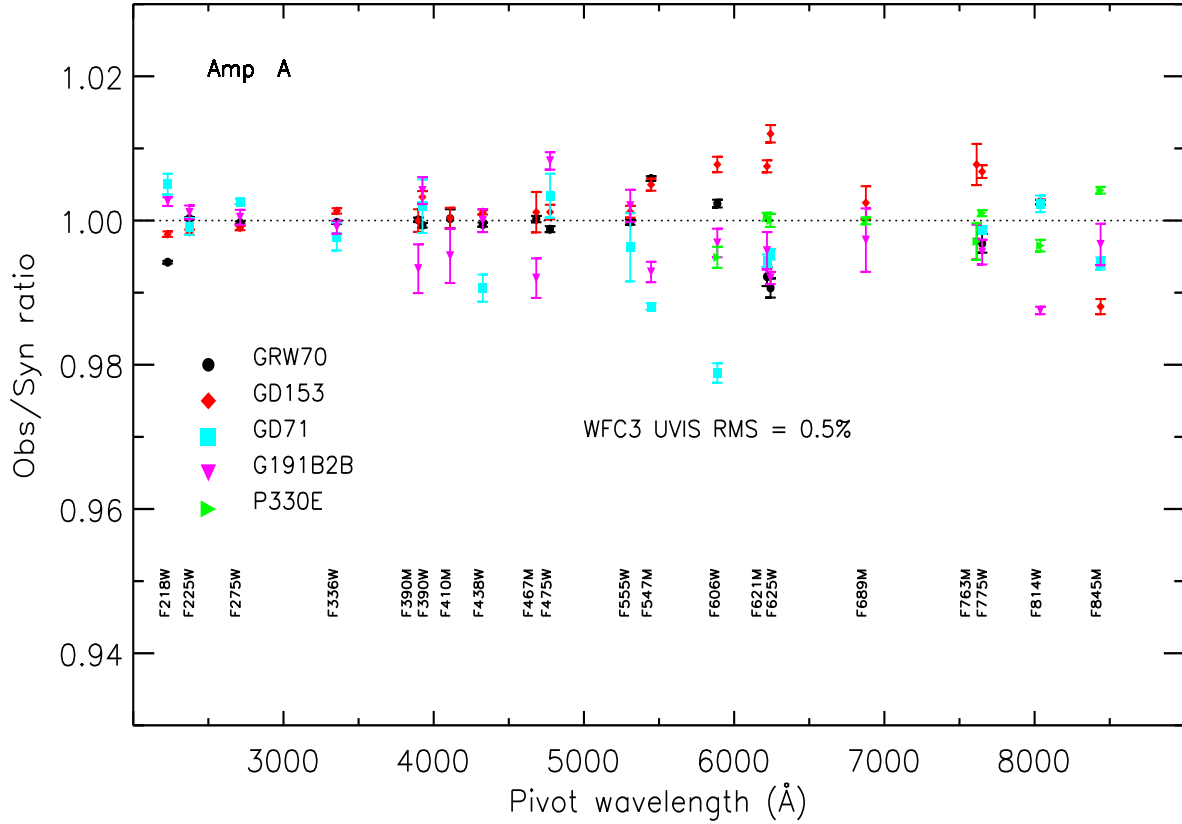


Figure 14: Observed over synthetic count rates for WFC3 UVIS1 (Amp A) wide- and medium-band filters for the five standard stars used in the calibration as a function of the pivot wavelength. Error bars are displayed. Note that ratios for P330E were calculated for $\lambda > 6000\text{\AA}$ only.

multiplicative scalar correction to be applied to each filter curve. New filter curves were created, and named as *wfc3uvis1_FXXXX_008_syn.fits* and *wfc3uvis2_FXXXX_008_syn.fits*, and used to calculate the final synthetic count rates for each detector, filter and standard star. These new filter curves provide count rates as observed at the reference epoch. Time-dependent filter curves are also created, *wfc3uvis1_FXXXX_mjd_008_syn.fits* and *wfc3uvis2_FXXXX_mjd_008_syn.fits*, which provide the count rates as expected at different epochs. Note that when using *Pysynphot* to derive count rates at different epochs for a target, the code interpolates between two consecutive MJD values included in the throughput tables. If the requested epoch is outside the current lifetime of WFC3, the values will be extrapolated in the future or in the past. The extrapolation to MJD values before the reference epoch, i.e. before WFC3 was launched, are not reliable and should not be used in simulations.

Figs. 14 and 15 show the observed over synthetic count rates for the five standard stars and the wide- and medium-band filters obtained with the new filter curves. The ratio values cluster around 1.0 as expected, with a RMS of 0.5% for both detectors.

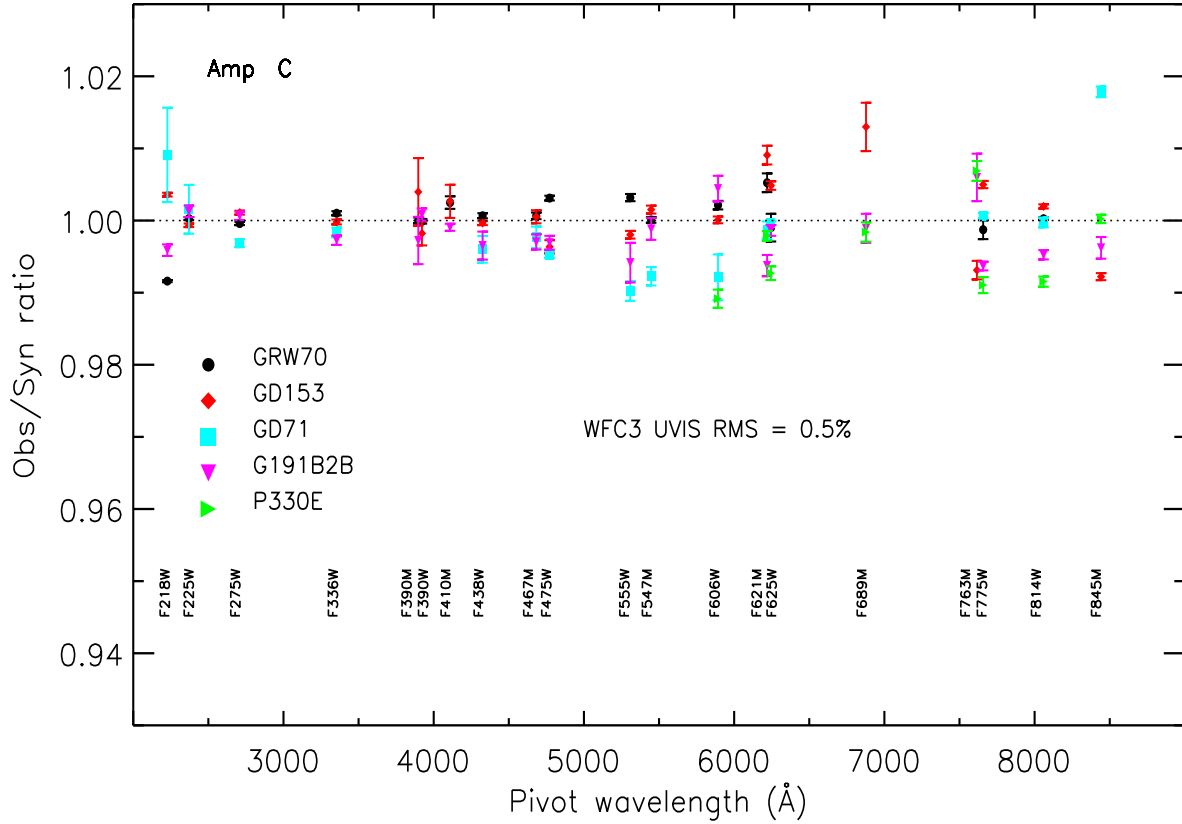


Figure 15: Same as Fig. 14 but for WFC3 UVIS2 (Amp C) filters.

5.1 Quad filters

In the case of the quad filters, not enough measurements of the standard stars are available to determine slopes for the sensitivity changes with time. Therefore, we use the available photometry to calculate the weighted mean count rates for each star in each filter and assumed the same reference epoch as for the other filters. New synthetic count rates are calculated by using the new SEDs and the old in-flight correction (*wfc3_uvis_cor_003_syn.fits*), old aperture corrections (*wfc3_uvis_aper_002_syn.fits*) and old filter curves (*wfc3_uvis_FQXXX_004_syn.fits* or *wfc3_uvis_FQXXX_005_syn.fits*). It is worth noting that inverse sensitivities for quad filters are calculated for UVIS1 only. The same procedure is used to derive multiplicative scalar factors to create new filter curves. These are also named as *wfc3_uvis_FQXXX_008_syn.fits*.

6 Calculating the inverse sensitivities

We now have updated synthetic count rates and time-dependent corrected photometry for the five standard stars for both detectors and the 42 full-frame filters plus the 20 quad filters. In order to derive new inverse sensitivities we followed the method of Bohlin et al. (2014, 2020) and DE16. The instrument count rate, N_e , in photoelectrons per second, is defined as:

$$N_e = \frac{A}{hc} \int F_\lambda \cdot \lambda \cdot R \cdot d\lambda \quad (1)$$

where A is the telescope collecting area, h is the Planck constant, c is the speed of light, R is the system throughput and F_λ is the source spectral flux density in $\text{erg} \cdot \text{s}^{-1} \cdot \text{cm}^{-2} \cdot \text{\AA}^{-1}$.

The inverse sensitivity S , which is defined as the flux that gives 1 count/s, can now be written as:

$$S = \frac{hc}{A \cdot \int \lambda \cdot R \cdot d\lambda} \quad (2)$$

and has units of $\text{erg} \cdot \text{cm}^{-2} \cdot \text{\AA}^{-1} / \text{e}^-$. The flux is thus:

$$F = S \cdot N_e = S \cdot C \quad (3)$$

where C is the source count rate in e^-/s . We can derive the inverse sensitivity by inverting the last relation:

$$S = C/F \quad (4)$$

where C is available from the observations of the standard stars and F is provided by the *Pysynphot* simulations performed with the updated corrections and filter curves.

Inverse sensitivities at *infinity* are derived for UVIS1 and UVIS2 and indicated in the image header as the PHFTLAM1 and PHTFLAM2 keywords, respectively. The PHOTFLAM keyword is set to the value of PHTFLAM1, except for the UV filters (see below). The ratio of the UVIS2 and UVIS1 inverse sensitivities (S_2/S_1 or PHTFLAM2/PHTFLAM1) is indicated in the image header by the keyword PHTRATIO (see Section 6.1). As defined in DE17, the value of the UVIS1 inverse sensitivity is modified (S'_1) for the UV filters, namely $F218W$, $F225W$, $F275W$ and $F200LP$, such that the ratio of the inverse sensitivities, PHTRATIO (S_2/S'_1) is equal to the count rate ratio, C_1/C_2 . This equivalency only holds for hot stars, $T_{eff} \gtrsim 30,000\text{K}$, since cooler stars have a largely different SEDs in the UV regime, and the response of the detector + filter system will be different for these sources (Calamida et al. 2018). Therefore, magnitude offsets for the UV filters as a function of the source color need be applied to magnitudes measured on UVIS2 to transform the photometry to the UVIS1 photometric system. Corrections are currently available in Calamida et al.; however, new corrections will be provided in the future based on the new inverse sensitivities presented in this ISR.

The new inverse sensitivities for UVIS1 and UVIS2 at the reference epoch, MJD = 55008 (June 26, 2009) are listed in Tables 6 (42 full-frame filters) and Table 7 (20 quad filters), and provided at the WFC3 Photometric Calibration web-page⁹. Inverse sensitivities may also be computed 'on-the-fly' for any observation epoch by using *synphot* and the new set of filter curves: an example notebook tutorial is provided at the same webpage.

⁹<https://www.stsci.edu/hst/instrumentation/wfc3/data-analysis/photometric-calibration/uvis-photometric-calibration>

Table 6: New inverse sensitivity values (PHOTFLAM) and ZPs in different photometric systems for UVIS1 (Amp A) and UVIS2 (Amp C) 42 full-frame filters calculated at the reference epoch MJD = 55008 (June 26, 2009). Errors are also listed.

Filter	Pivot (Å)	PHOTBW (Å)	ZP _{AB} (Mag)	ZP _{Vega} (Mag)	ZP _{ST} (Mag)	ZP _{ERR} (Mag)	PHOTFLAM (erg/cm ² /Å/s)	PHOTFLAM _{ERR} (erg/cm ² /Å/s)
UVIS1 (Amp A)								
F200LP	4971.86	1742.20	27.3356	26.8857	27.1261	0.0128	5.1234e-20	6.0032e-22
F218W	2228.04	128.94	22.9368	21.2726	20.9843	0.0072	1.4664e-17	9.6609e-20
F225W	2372.05	177.43	24.0631	22.4257	22.2467	0.0015	4.5849e-18	6.2529e-21
F275W	2709.69	164.43	24.1569	22.6759	22.6294	0.0017	3.2227e-18	5.1180e-21
F280N	2832.86	200.69	20.9180	19.5016	19.4871	0.0085	5.8231e-17	4.5543e-19
F300X	2820.47	316.56	24.9638	23.5611	23.5234	0.0024	1.4147e-18	3.1311e-21
F336W	3354.49	158.42	24.6908	23.5260	23.6269	0.0018	1.2860e-18	2.1606e-21
F343N	3435.15	86.71	23.8868	22.7517	22.8745	0.0016	2.5716e-18	3.6774e-21
F350LP	5873.87	1490.06	26.9647	26.8116	27.1173	0.0050	5.1653e-20	2.4005e-22
F373N	3730.17	18.34	21.9076	21.0354	21.0742	0.0090	1.3499e-17	1.1206e-19
F390M	3897.24	65.48	23.6216	23.5457	22.8834	0.0052	2.5506e-18	1.2257e-20
F390W	3923.69	291.27	25.3725	25.1735	24.6489	0.0032	5.0170e-19	1.4587e-21
F395N	3955.19	26.29	22.6678	22.7115	21.9616	0.0024	5.9616e-18	1.3191e-20
F410M	4108.99	57.03	23.5959	23.7699	22.9726	0.0038	2.3495e-18	8.2162e-21
F438W	4326.23	197.31	24.8367	25.0015	24.3252	0.0060	6.7593e-19	3.7819e-21
F467M	4682.58	68.42	23.6935	23.8567	23.3539	0.0062	1.6536e-18	9.5492e-21
F469N	4688.10	19.97	21.8160	21.9825	21.4790	0.0029	9.2985e-18	2.5187e-20
F475W	4773.10	421.30	25.7039	25.8094	25.4058	0.0055	2.4984e-19	1.2504e-21
F475X	4940.72	660.68	26.1558	26.2131	25.9327	0.0017	1.5379e-19	2.3980e-22
F487N	4871.38	21.71	22.2269	22.0479	21.9731	0.0039	5.8987e-18	2.1052e-20
F502N	5009.64	26.96	22.3262	22.4190	22.1332	0.0050	5.0899e-18	2.3595e-20
F547M	5447.50	206.24	24.7550	24.7583	24.7440	0.0100	4.5959e-19	4.2627e-21
F555W	5308.43	517.49	25.8097	25.8379	25.7425	0.0028	1.8324e-19	4.6668e-22
F600LP	7468.12	945.89	25.8820	25.5487	26.5560	0.0070	8.6611e-20	5.5311e-22
F606W	5889.17	657.20	26.0872	26.0039	26.2454	0.0129	1.1529e-19	1.3885e-21
F621M	6218.85	185.65	24.6124	24.4620	24.8889	0.0070	4.0217e-19	2.5967e-21
F625W	6242.56	451.28	25.5247	25.3736	25.8095	0.0094	1.7225e-19	1.4834e-21
F631N	6304.29	41.60	21.8849	21.7232	22.1910	0.0114	4.8259e-18	5.0616e-20
F645N	6453.59	41.45	22.2434	22.0478	22.6004	0.0039	3.3101e-18	1.1955e-20
F656N	6561.37	41.77	20.4221	19.8404	20.8151	0.0385	1.7137e-17	5.9545e-19
F657N	6566.63	41.00	22.6585	22.3324	23.0531	0.0043	2.1815e-18	8.7084e-21
F658N	6584.02	148.71	21.0271	20.6717	21.4275	0.0177	9.7468e-18	1.5697e-19
F665N	6655.88	42.19	22.7339	22.4901	23.1578	0.0096	1.9808e-18	1.7401e-20
F673N	6765.94	41.94	22.5877	22.3424	23.0473	0.0069	2.1931e-18	1.3993e-20
F680N	6877.60	112.01	23.8182	23.5546	24.3133	0.0140	6.8336e-19	8.9134e-21
F689M	6876.75	207.61	24.4777	24.1950	24.9725	0.0028	3.7238e-19	9.6694e-22
F763M	7614.37	229.42	24.2260	23.8366	24.9421	0.0068	3.8296e-19	2.3862e-21
F775W	7651.36	419.72	24.8714	24.4800	25.5981	0.0048	2.0930e-19	9.1984e-22
F814W	8039.06	666.76	25.1272	24.6985	25.9612	0.0075	1.4980e-19	1.0373e-21
F845M	8439.06	260.30	23.8216	23.3150	24.7610	0.0091	4.5246e-19	3.8212e-21
F850LP	9176.13	470.53	23.8557	23.3253	24.9769	0.0066	3.7086e-19	2.2782e-21
F953N	9530.58	71.19	20.4250	19.8019	21.6285	0.0111	8.1018e-18	8.2727e-20
UVIS2 (Amp C)								
F200LP	4875.10	1725.22	27.3803	26.9000	27.1282	0.0127	5.1134e-20	5.9509e-22
F218W	2223.72	124.92	23.2115	21.5463	21.2548	0.0106	1.1430e-17	1.1093e-19
F225W	2358.39	173.15	24.2791	22.6377	22.4501	0.0012	3.8015e-18	4.2937e-21
F275W	2703.30	165.58	24.2223	22.7373	22.6897	0.0021	3.0488e-18	5.9952e-21

F280N	2829.98	202.41	20.9303	19.5123	19.4972	0.0182	5.7693e-17	9.5770e-19
F300X	2805.84	316.95	25.0513	23.6394	23.5995	0.0117	1.3186e-18	1.4264e-20
F336W	3354.65	158.34	24.7185	23.5538	23.6547	0.0022	1.2535e-18	2.5211e-21
F343N	3435.19	86.65	23.9236	22.7885	22.9113	0.0042	2.4858e-18	9.6503e-21
F350LP	5851.15	1483.02	26.9356	26.7802	27.0798	0.0048	5.3469e-20	2.3475e-22
F373N	3730.16	18.29	21.9350	21.0628	21.1016	0.0051	1.3163e-17	6.1663e-20
F390M	3897.00	65.47	23.6375	23.5611	22.8992	0.0037	2.5138e-18	8.5689e-21
F390W	3920.72	291.16	25.3811	25.1779	24.6559	0.0017	4.9849e-19	7.8536e-22
F395N	3955.15	26.30	22.6700	22.7139	21.9638	0.0034	5.9495e-18	1.8615e-20
F410M	4108.88	56.96	23.5944	23.7683	22.9709	0.0029	2.3530e-18	6.3673e-21
F438W	4325.14	197.42	24.8343	24.9990	24.3223	0.0034	6.7777e-19	2.1424e-21
F467M	4682.60	68.37	23.6984	23.8616	23.3588	0.0024	1.6461e-18	3.7092e-21
F469N	4688.10	20.07	21.8199	21.9864	21.4828	0.0089	9.2649e-18	7.6216e-20
F475W	4772.17	421.76	25.6961	25.8017	25.3977	0.0048	2.5172e-19	1.1204e-21
F475X	4937.41	661.13	26.1519	26.2092	25.9273	0.0045	1.5455e-19	6.4132e-22
F487N	4871.38	21.84	22.2413	22.0624	21.9875	0.0165	5.8199e-18	8.8914e-20
F502N	5009.63	27.10	22.3215	22.4143	22.1285	0.0048	5.1120e-18	2.2581e-20
F547M	5447.24	206.18	24.7592	24.7625	24.7480	0.0050	4.5792e-19	2.1269e-21
F555W	5307.91	517.13	25.7962	25.8245	25.7288	0.0076	1.8556e-19	1.3004e-21
F600LP	7453.66	937.10	25.8573	25.5254	26.5271	0.0090	8.8952e-20	7.3298e-22
F606W	5887.71	656.93	26.0785	25.9954	26.2361	0.0079	1.1629e-19	8.5554e-22
F621M	6219.16	185.71	24.6065	24.4560	24.8831	0.0068	4.0434e-19	2.5181e-21
F625W	6241.96	451.09	25.5247	25.3736	25.8092	0.0049	1.7231e-19	7.8251e-22
F631N	6304.28	42.39	21.8900	21.7283	22.1961	0.0102	4.8033e-18	4.4718e-20
F645N	6453.58	42.24	22.2381	22.0425	22.5951	0.0050	3.3263e-18	1.5421e-20
F656N	6561.36	42.44	20.4568	19.8751	20.8497	0.0126	1.6600e-17	1.9100e-19
F657N	6566.60	41.07	22.6580	22.3319	23.0527	0.0051	2.1824e-18	1.0186e-20
F658N	6583.92	151.15	21.0376	20.6820	21.4379	0.0080	9.6562e-18	7.1081e-20
F665N	6655.84	42.26	22.7212	22.4775	23.1452	0.0062	2.0041e-18	1.1303e-20
F673N	6765.91	42.13	22.5625	22.3171	23.0220	0.0121	2.2447e-18	2.4847e-20
F680N	6877.41	112.06	23.7974	23.5339	24.2925	0.0065	6.9662e-19	4.1363e-21
F689M	6876.50	207.84	24.4682	24.1855	24.9630	0.0100	3.7566e-19	3.4228e-21
F763M	7612.74	228.87	24.2051	23.8160	24.9208	0.0087	3.9054e-19	3.1189e-21
F775W	7648.30	418.28	24.8610	24.4700	25.5868	0.0067	2.1149e-19	1.3204e-21
F814W	8029.32	663.97	25.1118	24.6841	25.9431	0.0056	1.5232e-19	7.8754e-22
F845M	8437.27	259.71	23.8125	23.3060	24.7515	0.0123	4.5641e-19	5.1436e-21
F850LP	9169.94	466.6	23.8099	23.2799	24.9297	0.0076	3.8736e-19	2.7041e-21
F953N	9530.50	72.85	20.3831	19.7601	21.5866	0.0122	8.4191e-18	9.5450e-20

6.1 Detector sensitivity ratios

We use the new inverse sensitivities to calculate updated detector sensitivity ratio $\text{PHTRATIO} = \text{PHTFLAM2}/\text{PHTFLAM1}$ values. These values are used by the WFC3 pipeline, *calwf3*, to flux correct UVIS2 to UVIS1. Note that this correction is performed by default and allows users to apply only one inverse sensitivity value, PHTFLAM1 , to calibrate the photometry. However, if observations are done by using a UVIS2 sub-array, the flux correction can be avoided by setting $\text{FLUXCORR} = \text{OMIT}$ in the image header and re-running *calwf3* on the raw images. In this case, the PHTFLAM2 values in the image header should be used to calibrate the photometry.

Due to the new inverse sensitivities being time-dependent, PHTRATIO varies with the epoch

Table 7: New inverse sensitivity values (PHOTFLAM) and ZPs in different photometric systems for the 20 quad filters calculated at the reference epoch MJD = 55008 (June 26, 2009). Errors are also listed.

Filter	Pivot (Å)	PHOTBW (Å)	ZP_{AB} (Mag)	ZP_{Vega} (Mag)	ZP_{ST} (Mag)	ZP_{ERR} (Mag)	PHOTFLAM (erg/cm ² /Å/s)	PHOTFLAM _{ERR} (erg/cm ² /Å/s)
FQ232N	2432.22	263.50	20.4123	18.8028	18.6502	0.0064	1.2587e-16	7.4676e-19
FQ243N	2476.32	193.97	20.7378	19.1082	19.0148	0.0129	9.0301e-17	9.5288e-18
FQ378N	3792.41	32.14	22.7507	22.2919	21.9532	0.0136	6.0299e-18	3.8173e-19
FQ387N	3873.66	15.01	21.3399	21.2738	20.5884	0.0136	2.0928e-17	2.8522e-19
FQ422N	4219.21	38.33	22.6725	22.9269	22.1066	0.0185	5.1880e-18	5.3523e-20
FQ436N	4367.16	22.82	21.6299	21.6775	21.1389	0.0081	1.2684e-17	3.1092e-19
FQ437N	4371.04	21.60	21.2682	21.3942	20.7790	0.0369	1.7282e-17	5.5396e-19
FQ492N	4933.44	35.18	22.8676	22.9380	22.6413	0.0073	3.1887e-18	1.5797e-20
FQ508N	5091.05	42.37	22.8805	22.9579	22.7225	0.0389	2.9976e-18	1.5032e-19
FQ575N	5757.69	42.20	20.5297	20.4709	20.6388	0.0537	2.0246e-17	7.3602e-19
FQ619N	6198.52	36.45	21.9403	21.7985	22.2097	0.0160	4.7187e-18	6.4863e-20
FQ634N	6349.21	43.00	21.9575	21.7809	22.2790	0.0307	4.4312e-18	7.6042e-20
FQ672N	6716.38	70.00	20.3946	20.1585	20.8382	0.0960	1.5193e-17	1.6124e-18
FQ674N	6730.68	39.20	20.6923	20.4535	21.1406	0.0403	1.6657e-17	6.8407e-18
FQ727N	7275.23	63.22	21.5808	21.2474	22.1979	0.0676	4.7367e-18	2.6141e-19
FQ750N	7502.50	28.12	21.5024	21.1309	22.1864	0.0561	4.6196e-18	2.9526e-19
FQ889N	8892.15	55.49	21.0572	20.5360	22.1102	0.0181	5.0706e-18	5.8733e-19
FQ906N	9057.76	57.30	20.9512	20.4312	22.0443	0.0500	5.3340e-18	2.4683e-19
FQ924N	9247.59	46.28	20.7532	20.1576	21.8913	0.0500	6.3554e-18	2.9059e-18
FQ937N	9372.42	54.80	20.6478	20.1671	21.8150	0.0045	7.2367e-18	4.2433e-19

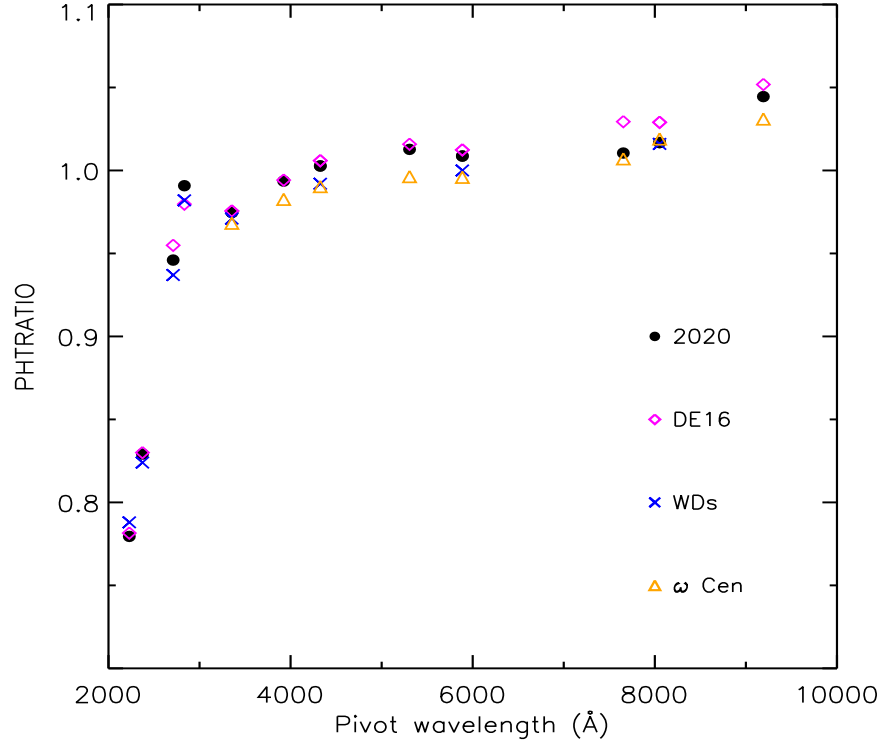


Figure 16: Comparison of old (DE16, magenta diamond) and new (2020, filled black circle) synthetic detector sensitivity ratios, PHTRATIO, with observed values computed from WD (blue cross) and ω Cen (orange triangle) observations. See text for more details.

Table 8: PHTRATIO values (PHTFLAM2/PHTFLAM1) for the WFC3-UVIS 42 full-frame filters derived from synthetic photometry by using the new (syn_2020) and the old (syn_DE16) calibration *Pysynphot* files, and by using observations of standard WDs and ω Cen.

Filter	Pivot	PHTRATIO _{syn_2020}	PHTRATIO _{syn_DE16}	PHTRATIO _{WDs}	PHTRATIO _{ωCen}
F200LP	4971.86	0.998	1.0023
F218W	2228.04	0.779	0.7815	0.788	...
F225W	2372.05	0.829	0.8300	0.824	...
F275W	2709.69	0.946	0.9549	0.937	...
F280N	2832.86	0.991	0.9797	0.982	...
F300X	2820.47	0.932	0.9350
F336W	3354.49	0.975	0.9756	0.971	0.968
F343N	3435.15	0.967	0.9690
F350LP	5873.87	1.035	1.0316
F373N	3730.17	0.975	0.9663
F390M	3897.24	0.985	0.9870
F390W	3923.69	0.994	0.9942	...	0.983
F395N	3955.19	0.998	1.0031
F410M	4108.99	1.001	1.0022
F438W	4326.23	1.003	1.0059	0.992	0.990
F467M	4682.58	0.995	0.9979
F469N	4688.10	0.996	1.0082
F475W	4773.10	1.007	1.0126
F475X	4940.72	1.005	1.0121
F487N	4871.38	0.987	1.0028
F502N	5009.64	1.004	1.0187
F547M	5447.50	0.996	1.0158
F555W	5308.43	1.013	1.0013
F600LP	7468.12	1.027	1.0335
F606W	5889.17	1.009	1.0124	1.000	0.996
F621M	6218.85	1.005	1.0140
F625W	6242.56	1.000	1.0169
F631N	6304.29	0.995	1.0049
F645N	6453.59	1.005	1.0111
F656N	6561.37	0.969	1.0008
F657N	6566.63	1.000	1.0049
F658N	6584.02	0.991	1.0069
F665N	6655.88	1.012	1.0135
F673N	6765.94	1.023	1.0202
F680N	6877.60	1.019	1.0074
F689M	6876.75	1.009	1.0139
F763M	7614.37	1.020	1.0340
F775W	7651.36	1.010	1.0294	...	1.007
F814W	8039.06	1.017	1.0290	1.016	1.019
F845M	8439.06	1.009	1.0171
F850LP	9176.13	1.044	1.0518	...	1.031
F953N	9530.58	1.039	1.0231

of observations as well. We calculated PHTRATIO by using the PHTFLAM1 and PHTFLAM2 values at the reference epoch and results are listed in Table 8, with a comparison to the DE16 PHTRATIO values. We compare the new values with PHTRATIO calculated by using the photometry of standard star WDs dithered on the image and observed between 2010 and 2014 (Mack et al. 2015) and photometry from dithered images of ω Cen observed between 2009 and 2011 (Mack et al. 2013, 2016). Note that these PHTRATIO values are calculated for a 10 pixel aperture radius and no time-dependent sensitivity correction is applied; however, the observations were mostly done at the beginning of WFC3 lifetime (2009 – 2014) so the total sensitivity losses are $\approx 1\%$ at most, depending on the filter. The observed PHTRATIO values derive from WD and ω Cen photometry are shown in Fig. 16, where the new and old synthetic PHTRATIO values are also plotted for the same filters as a function of the pivot wavelength. Table 8 and Fig. 16 show that the new

PHTRATIO values agree very well with those obtained from both WD and ω Cen observations, and show improvements in several filters from the old PHTRATIO values which did not include any time-dependent sensitivity correction.

7 Comparison with the old inverse sensitivity values

We compare the new inverse sensitivities (zero points, ZPs) with the those from the 2017 calibration. The latter ZPs were calculated by using the previous CALSPEC SEDs (v10) and 6 years of data available for the standard stars (2009 – 2015): these measurements were simply averaged without normalizing for the sensitivity changes with time. This resulted in different reference epochs per filters; additionally, the 2017 calibration did not account for differences in the observed count rates due to flat field errors. In this work, the inverse sensitivities are derived using the new CALSPEC SEDs for the standard stars (v11), and 10 years of available data (2009 – 2019). The photometric measurements of the standard stars are now normalized to a single reference epoch and weighted for the errors and the number of measurements.

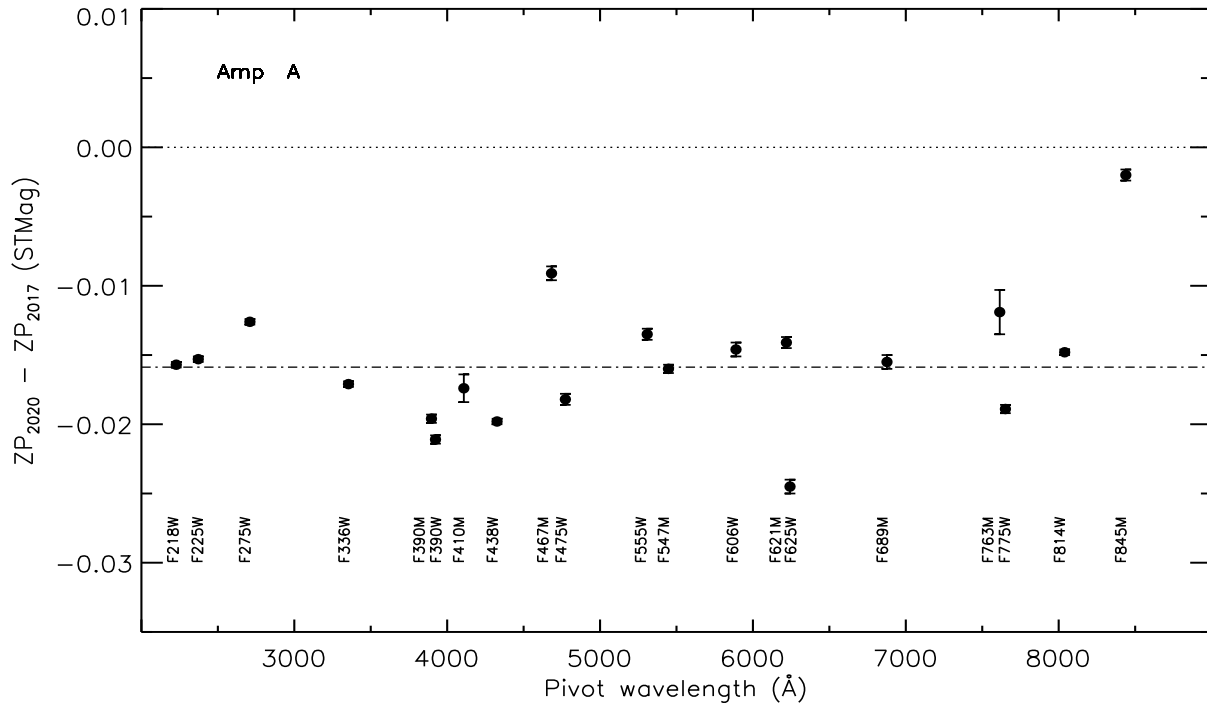


Figure 17: Comparison between the new (2020) and old (2017) ZPs for WFC3 UVIS1 (Amp A) in the ST photometric system for the wide- and medium-band filters over the entire WFC3 UVIS wavelength range.

Fig. 17 shows the comparison between new (2020) and old (2017) ZPs as a function of pivot wavelength for the wide- and medium-band UVIS1 filters. The ZPs differ on average by $\approx 1.5\%$, with the new ZPs being brighter compared to the old ones. This is mostly due to the reference flux of Vega being $\approx 1\%$ brighter, and to the standard star photometry being corrected for losses in sensitivity. A similar comparison holds for the UVIS2 filters as shown in Fig. 18, where the

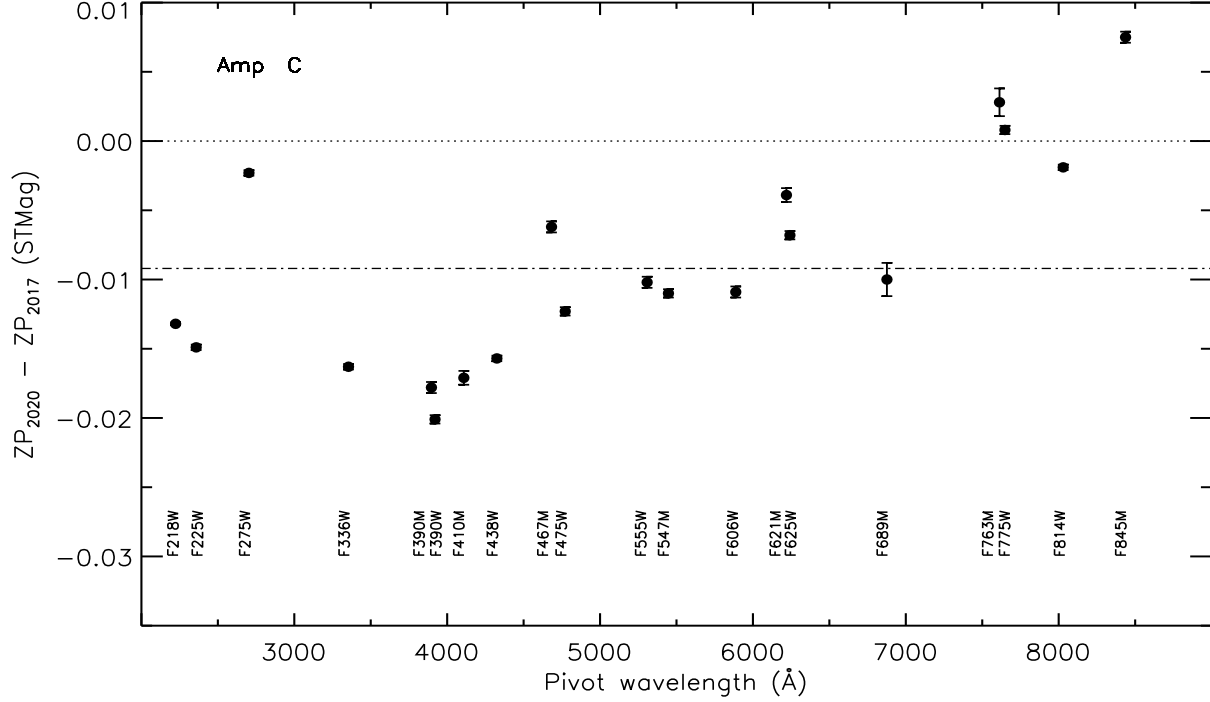


Figure 18: Same as Fig. 17 but for WFC3 UVIS2 (Amp C) detector.

ZPs differ on average by $\approx 0.9\%$. It is worth noting that the difference between old and new ZPs for the UVIS2 detector shows a slope between $4,000 < \lambda < 8,000 \text{ Å}$ that is not clearly seen for UVIS1 values. This difference between the two detectors may be due to how the five standard star measurements were collected between 2009 and 2019: for most filters, Amp A has more observations at the beginning, 2009-2010, and throughout WFC3 lifetime compared to Amp C, which has less and more sparse measurements. Since the old ZPs were calculated by simply averaging the photometry of the standard stars over the 2009 – 2015 time interval, without applying any time correction, the ZP values for UVIS1 resulted to be centered on earlier epochs compared to values for UVIS2.

8 Conclusions

In this ISR we derived new time-dependent inverse sensitivities for the two WFC3-UVIS detectors, UVIS1 and UVIS2, for all 42 full-frame filters. They provide a photometric internal precision of $\lesssim 0.5\%$ for wide-, medium-, and narrow-band filters, with a significant improvement compared to the old values, where the precision was $\lesssim 1\%$ for wide-, $\lesssim 2\%$ for medium-, and $\lesssim 5 - 10\%$ for narrow-band filters.

Major changes of the new inverse sensitivities compared to the 2017 values can be summarized as follows:

- 1) The new values are based on new SEDs for the standard stars and a new reference flux for Vega (CALSPEC v11, Bohlin et al. 2020);
- 2) EE values for a few filters were updated by using the time-sensitivity corrections and a new method for drizzling the standard star images. These were used in the computation of the new

inverse sensitivities;

3) Four extra years (2015 – 2019) of standard star photometry was used;

4) Time-dependent corrections were calculated and standard star photometry was corrected for the sensitivity changes before deriving the inverse sensitivities. Also, the standard star observed count rates were weighted according to their photometric errors and number of collected measurements.

We also provided new inverse sensitivities for the WFC3-UVIS 20 quad filters by using the new SEDs for the standard stars and the reference Vega flux. These values do not have a time-sensitivity correction, since not enough observations were available to calculate a sensitivity change rate.

New in-flight correction files, new aperture corrections, and new filter throughputs for all filters were delivered to the CDBS database and can be downloaded from the CALSPEC web-page¹⁰, and used in *synphot* simulations (see Table 5 for a list of the file names). A new IMPHTTAB was also delivered (*51c1638pi_imp.fits*) and all WFC3-UVIS data were reprocessed through the new version of the pipeline, *calwf3_v3.5.1*.

The new time-dependent photometry keyword values (PHOTFLAM, PHTFLAM1, PHTFLAM2 and PHTRATIO) will be populated in the image headers for data retrieved after October 15, 2020. Therefore, we recommend the user to retrieve again data collected before this date so that their headers will be populated with the latest time-dependent inverse sensitivity values.

The WFC3-UVIS photometric calibration web-page¹¹ provides the new inverse sensitivity values calculated at the reference epoch, i.e. MJD = 55008 (June 26, 2009). Values of the inverse sensitivities for both detectors at each observing epoch can be found in the image header. However, at the same web-page, we also provide a tutorial (Jupyter notebook) for running *synphot* with the new filter curves in order to derive the inverse sensitivity and ZP values for any detector, observation epoch, filter or aperture. A second Jupiter notebook describes how to use the new time-dependent solutions to work with UVIS data obtained at different observation dates.

Acknowledgements

This work has been done with the contribution of all members of the WFC3 Photometric group that we acknowledge here and as co-authors of this ISR. We would like to thank Harish Khandrika for helping with testing the new time-dependent inverse sensitivities, and Catherine Martlin for delivering the new IMPHTTAB and all the *synphot* files. We also thank the reviewer of this document, Kailash Sahu, and the helpful comments from Joel Green.

¹⁰<https://www.stsci.edu/hst/instrumentation/reference-data-for-calibration-and-tools/astronomical-catalogs/calspec>

¹¹<https://www.stsci.edu/hst/instrumentation/wfc3/data-analysis/photometric-calibration/uvis-photometric-calibration>

References

- Bohlin, R. 2014, AJ, 147, 127
- Bohlin, R., Hubeny, I., Rauch, T. 2020, AJ, 160, 21
- Brown, T., WFC3 ISR 2008-49, "WFC3 TV3 Testing: Red Leak Checks for the UV Filters"
- Calamida, A., Mack, J., Deustua, S., Sabbi, E. 2018, WFC3 ISR 2018-08, "WFC3 color term transformations for UV filters"
- Carlberg, J.K. Monroe, T., STIS ISR 2017-06, "Updated Time Dependent Sensitivity Corrections for STIS Spectral Modes"
- Deustua, S., Mack, J., Bowers, A.S., Baggett, S., Bajaj, V., Dahlen, T., Durbin, M., Gosmeyer, C., Gunning, H., Hammer, D., Hartig, G., Khandrika H., MacKenty, J., Ryan, R., Sabbi, E., Sosey, M. 2016, WFC3 ISR 2016-03, "UVIS 2.0 Chip-dependent Inverse Sensitivity Values" (DE16)
- Deustua, S. Bohlin, R. C., Mack, J., Bajaj, V. 2017 WFC3 ISR 2017-07, "WFC3 Chip Dependent Photometry with the UV filters"
- Deustua, S, Mack, J., Bajaj, V., Khandrika, H. 2017 WFC3 ISR 2017-14, "WFC3/UVIS Updated 2017 Chip-Dependent Inverse Sensitivity Values" (DE17)
- Gosmeyer, C. M., Baggett, S. 2016, WFC3 ISR 2016-17, "WFC3/UVIS External CTE Monitor: Single-Chip CTE measurements"
- Hartig, G.F. 2009, WFC3 ISR 2009-38, "WFC3 SMOV Programs 11436/8: UVIS On-orbit PSF Evaluation"
- Kalirai, J. S., MacKenty, J., Rajan, A., Bagget, S., Bohlin, R., Brown, T., Deustua, S., Kimble, R. A., Riess, A., Sabbi, E., and the WFC3 team, 2009, WFC3 ISR 2009-31, "WFC3 SMOG Proposal 11450: The Photometric Performance and Calibration of WFC3/UVIS"
- Kalirai, J. S., Cox, C., Dressel, L., Fruchter, A., Hack, W., Kozhurina-Platais, and Mack, J., 2010, WFC3 ISR 2010-08, "WFC3 Pixel Area Maps"
- Khandrika, H., Deustua, S, Mack, J. 2018, WFC3 ISR 2018-16, "'WFC3-UVIS - Temporal and Spatial Variations in Photometry"
- Lim, P. L., Diaz, R. I., & Laidler, V. 2015, "PySynphot User's Guide"
- Mack, J., Sabbi, E., Dahlen, T. 2013, WFC3 ISR 2013-10, "In-flight Corrections to the WFC3 UVIS Flat Fields"
- Mack, J., Rajan, A., Bowers, A. S. 2015, WFC3 ISR 2015-18, "Spatial Accuracy of the UVIS flat fields"

- Mack, J., Dahlen, T., Sabbi, E., Bowers, A. S. 2016, WFC3 ISR 2016-04, "UVIS 2.0: Chip-Dependent Flats"
- Mack, J. 2016, WFC3 ISR 2016-05, "UVIS 2.0: Ultraviolet flats"
- Shanahan, C., Gosmeyer, C. M., Baggett, S. 2017, WFC3 ISR 2017-15, "Update on the WFC3/UVIS Stability and Contamination Monitor"
- Shanahan, C., McCullough, P., Baggett, S. 2017, WFC3 ISR 2017-21, "Photometric Repeatability of Scanned Imagery: UVIS"
- Stetson, P. B., 1987, PASP, 99, 191, "DAOPHOT - A computer program for crowded-field stellar photometry"

Appendix

How to use the new ZPs

The new WFC3 processing pipeline, *calwf3_v3.5.1*, scales the UVIS2 detector to UVIS1. Therefore, users need to apply only one inverse sensitivity value, PHTFLAM1 (also available in the PHOTFLAM header keyword) to calibrate their photometry. However, if observations are done by using a UVIS2 sub-array, the flux correction can be avoided by setting FLUXCORR = OMIT in the image header and re-running *calwf3* on the raw images. In this case, the PHTFLAM2 values in the image header should be used to calibrate the photometry.

Photometry for images retrieved after October 15, 2020 or re-processed after this date, should be calibrated by using the new time-dependent UVIS1 inverse sensitivities available in the image header. In order to convert the provided PHOTFLAM values in ZPs in different photometric systems the user can use the following equations:

- for the ST photometric system:

$$ZP_{STMag} = -21.1 - 2.5 \times \log(PHOTFLAM) \quad (5)$$

- for the AB photometric system:

$$ZP_{ABMag} = -21.1 - 2.5 \times \log(PHOTFLAM) - 5 \times \log_{10}(PHOTPLAM) + 18.6921 \quad (6)$$

where PHOTPLAM is the filter bandwidth;

- for the Vega photometric system, the calculation of the ZP follows multiple steps. First, the user needs to calculate the flux of Vega as observed by the telescope, detector and filter, $FLAM_{Vega}$; to do this the new reference SED should be used, *alpha_lyr_stis_010.fits*, available from the CALSPEC database. Subsequently, the user has to calculate the ratio between the source observed flux and the Vega predicted flux. Magnitudes in the Vega photometric system are then defined as:

$$VegaMag = -2.5 \times \log_{10}(FLAM/FLAM_{Vega}) \quad (7)$$

A Jupyter notebook is provided on the WFC3-UVIS photometric calibration web-page¹² that shows how to calculate these three ZPs by using *synphot*, specifically *STSynphot*. A second notebook is also provided and shows how to use the new time-dependent solutions to work with UVIS data obtained at different observation dates.

Users should note that the final photometry for both detectors will be in the UVIS1 system. If the observed sources lie in the same detector, the color term is negligible ($< 1\%$), and no magnitude offset needs to be applied. However, due to the significantly different sensitivity of the UVIS1 and UVIS2 detector in the UV wavelength range, magnitude offsets for the UV filters as a function of the source color need be applied to magnitudes measured on UVIS2 to transform the photometry to the UVIS1 photometric system. Corrections are currently available in Calamida et al. (2018); however, new corrections will be provided in the future based on the new inverse sensitivities presented in this ISR as described in §6.

For users who require sub-percent photometric calibration accuracy, we recommend treating each UVIS detector separately when observing with the UV filters, i.e. *F218W*, *F225W*, *F275W*, and *F200LP*. UVIS1 magnitudes will be derived as before, by using PHOTFLAM, while the UVIS2 magnitudes will be derived by using PHTFLAM2. Note that in this case, the MAST downloaded images will have to be re-processed manually through the *calwf3_v3.5.1* pipeline omitting the flux correction, i.e. FLUXCORR must be set to OMIT in the image headers.

¹²<https://www.stsci.edu/hst/instrumentation/wfc3/data-analysis/photometric-calibration/uvis-photometric-calibration>